

RESEARCH ARTICLE SUMMARY

CELL BIOLOGY

Adipogenin promotes the development of lipid droplets by binding a dodecameric seipin complex

Chao Li†, Xue-Nan Sun†, *et al.*

Full article and list of author affiliations:
<https://doi.org/10.1126/science.adr9755>

INTRODUCTION: Adipogenin (Adig) is an 80–amino acid microprotein that is highly expressed in adipose tissues and steatotic liver. A previous genome-wide association study suggested that human *ADIG* is associated with blood leptin levels, highlighting its importance in energy metabolism. At the molecular level, Adig's function is largely unknown: No interacting proteins have been identified. At the cellular level, conflicting results have emerged regarding Adig's subcellular location and role in adipogenesis. In mice, the basis and extent of Adig's physiological effects remain elusive. Here, we systematically characterized Adig function at the molecular, cellular, and physiological levels.

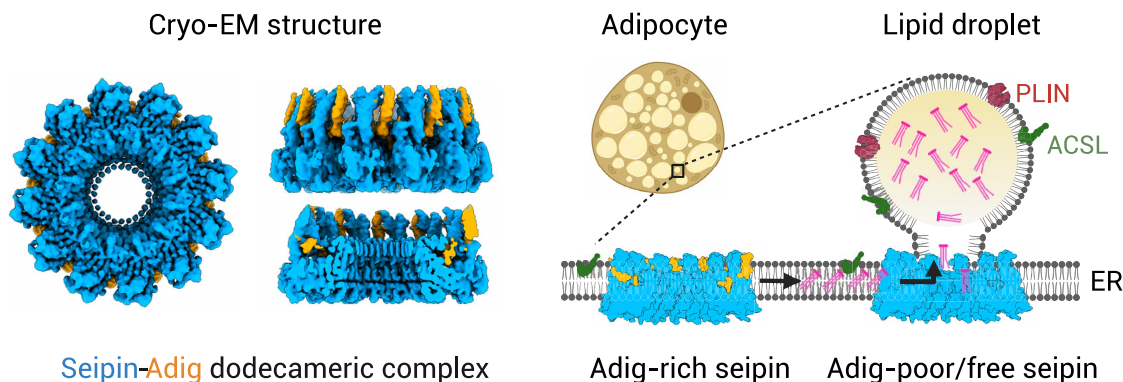
RATIONALE: Microproteins typically exert their functions by binding to larger proteins and regulating their activities. We pulled down Adig from adipocytes and identified its interacting proteins by mass spectrometry. Upon the identification of a seipin-Adig complex, we resolved its structure using cryo-electron microscopy (cryo-EM), enabling us to determine Adig's effect on seipin configuration at an atomic scale. Because seipin plays a vital role in lipid droplet (LD) formation and growth, we explored the function of the seipin-Adig complex in these processes. Moreover, we generated adipocyte-specific Adig overexpression and deletion mice to investigate Adig's effect on adipose tissue expansion and lipid metabolism *in vivo*.

RESULTS: We found that Adig is a highly conserved protein with a single transmembrane (TM) segment that localizes to the endoplasmic reticulum (ER). Notably, Adig and seipin can form a complex and stabilize each other. Cryo-EM analysis revealed two distinct oligomers: an undecameric seipin-alone complex at ~ 3.2 -Å overall resolution and a

dodecameric seipin-Adig complex at ~ 3.0 -Å overall resolution. In the seipin-Adig complex map, extra densities, corresponding to seipin and Adig TM domains, were observed. Multiple approaches, including high-resolution imaging, gel filtration, and molecular dynamics simulations, revealed that Adig could facilitate the assembly of dodecameric seipin complexes. Seipin complexes with varying Adig contents modulated LD formation and growth. The presence of the seipin-Adig complex altered triacylglycerol (TAG) flux in the ER, leading to the formation of fewer, but larger, LDs. Additionally, the ER-to-LD trafficking of select lipid-synthesizing enzymes was accelerated in Adig-expressing cells. In mice, Adig overexpression in adipocytes promoted LD enlargement and adipose tissue expansion, whereas Adig deletion decreased the amount of the seipin complexes in adipocytes and impaired TAG accumulation in brown adipose tissues.

CONCLUSION: In this study, we demonstrate that Adig complexes with seipin, forming a previously unrecognized dodecameric seipin complex. Furthermore, Adig stabilizes and promotes the assembly of this complex, thereby supporting LD growth in cells. In mice, modulating the expression of seipin-Adig complexes in adipose tissues by Adig overexpression or deletion substantially affects LD formation and expansion as well as lipid absorption by adipose tissues. This study reveals Adig as a key cofactor that modulates seipin function and fat storage in adipose tissue. We conclude that the oligomerization and function of seipin complexes can be modulated by Adig expression. □

Corresponding authors: Philipp E. Scherer (philipp.scherer@utsouthwestern.edu); Elina Ikonen (elina.ikonen@helsinki.fi) †These authors contributed equally to this work. Cite this article as C. Li *et al.*, *Science* 390, eadr9755 (2025). DOI: 10.1126/science.adr9755



Seipin-Adig complex promotes the development of lipid droplets. The seipin-Adig complex manifests as a distinctive oligomer of 12 subunits. Adig functions to maintain a pool of preassembled seipin-alone or seipin-Adig complexes, poised to facilitate the formation and expansion of LDs in adipose tissue. Mechanistically, the presence of seipin-Adig complexes enhances TAG flux into LDs, increases the ER-to-LD relocation of LD-targeting proteins, and may also promote lipid synthesis. ACSL and PLIN are LD targeting-proteins. ACSL, acyl-CoA synthetase long chain family member; PLIN, perilipin. [Figure created with BioRender.com]

CELL BIOLOGY

Adipogenin promotes the development of lipid droplets by binding a dodecameric seipin complex

Chao Li^{1†}, Xue-Nan Sun^{1†}, Jan-Bernd Funcke^{1‡}, Lauri Vanharanta^{2,3‡}, Xavier Prasanna⁴, Kaitlynn Gov⁵, Yan Li¹, Megan Virostek¹, Chanmin Joung¹, Nolwenn Joffin¹, Kristiina Kanerva^{2,3}, Abel Szkalitsy^{2,3}, Waldemar Kulig⁴, Leon Straub¹, Shihwei Chen¹, Joselin Velasco¹, Ayanna Cobb¹, Davide La Padula^{1,6}, May-Yun Wang¹, Toshiharu Onodera^{1,7}, Csaba Vörös^{2,3,8}, Dae-Seok Kim¹, Min Kim^{1,9}, Oleg Varlamov¹⁰, Yang Li¹¹, Chen Liu¹², Andrea R. Nawrocki¹³, Shangang Zhao^{1,14}, Da Young Oh¹, Zhao V. Wang^{15,16}, Ruth Gordillo¹, Joel M. Goodman¹⁷, R. Max Wynn^{1,18}, W. Mike Henne⁵, Ilpo Vattulainen⁴, Yan Han¹¹, Elina Ikonen^{2,3*}, Philipp E. Scherer^{1*}

The microprotein adipogenin (Adig) is predominantly expressed in adipose tissues. Here, we found that Adig interacts with seipin to form a stable, rigid complex. We present the structure of the seipin-Adig complex at an overall resolution of ~3.0 angstroms. The structure revealed that mammalian seipin assembles into two distinct oligomeric forms: undecamers and dodecamers. Adig selectively bound to the dodecameric form and enhanced seipin assembly by bridging and stabilizing adjacent subunits. Functionally, this complex promoted lipid droplet development at both early and late stages. In transgenic mice, adipocyte-specific overexpression of Adig increased fat mass and enlarged lipid droplets, whereas Adig deletion disrupted triglyceride accumulation in brown adipose tissues. Thus, Adig can modulate lipid storage through its structural and functional interactions with seipin.

Adipogenin (Adig) is an 80-amino acid microprotein, originally detected in steatotic livers upon peroxisome proliferator-activated receptor gamma (PPAR γ) overexpression in mice (1). Adig is highly expressed in adipose tissues and strongly up-regulated during adipogenesis (2–4). The phenotype of whole-body Adig deletion mice suggests that Adig may play a role in fat storage in adipose tissues (5). However, conflicting results have emerged regarding its intracellular localization and role in adipogenesis (2–5). Moreover, the molecular basis for Adig function remains largely unknown.

Seipin plays an essential and conserved role in lipid storage and lipid droplet (LD) development (6–10). Seipin elimination results in aberrations of LD size and number (11, 12). However, the precise mechanistic basis by which seipin mediates LD formation is unclear. One model to explain the process of LD growth and budding based on a cryo-electron microscopy (cryo-EM) structure of yeast seipin suggests

that the decameric seipin complex alternates between two conformations within the transmembrane (TM) domains during LD formation (13). However, how seipin functions in mammalian cells is unclear because the TM domains have not been structurally determined. Furthermore, the present yeast model requires the seipin complex to have an even number of subunits, which is incompatible with the reported undecameric seipin structure in humans (14). Here, we discovered a role of Adig in the assembly of seipin oligomers and LD development.

Adig is highly expressed in adipocytes and localized to the endoplasmic reticulum

Our interest in Adig was initiated when its expression was reported in steatotic livers (1). We found that *Adig* transcripts were highly enriched in mouse adipose tissues and testis (fig. S1A) and strongly induced during adipogenesis (fig. S1B). We raised antibodies against Adig to determine protein expression. Consistent with the mRNA expression, Adig protein was highly expressed in adipose tissues and testis (Fig. 1A). It was robustly up-regulated during adipogenesis in both brown (Fig. 1B) and white adipocytes (fig. S1C), concomitant with the induction of PPAR γ and Perilipin1. Furthermore, chromatin immunoprecipitation sequencing (ChIP-seq) databases showed that PPAR γ binds directly to the promoter region of *Adig* (and downstream of exon 1) in adipocytes (Fig. 1C). Indeed, the PPAR γ agonist rosiglitazone induced Adig expression (fig. S1D). Thus, PPAR γ controls the expression of Adig transcriptionally, thereby leading to high Adig protein expression in adipose tissues.

We next assessed the subcellular location of Adig because previous reports suggest different locations, including the plasma membrane (2), nuclei (3), and the surface of LDs (4). Sequence analysis across species revealed a long conserved hydrophobic α -helical stretch at the N terminus of Adig (Fig. 1, D and E), suggesting a transmembrane topology. To test this, we fused enhanced green fluorescent protein (EGFP) to either the N or C terminus of Adig and cotransfected it into HeLa cells with the endoplasmic reticulum (ER) marker ER-mCherry-KDEL or with the mitochondrial marker mito-mKeima (15). The localization of Adig-EGFP overlapped with that of the ER-mCherry-KDEL protein (Fig. 1F), but not with mito-mKeima (fig. S1E). EGFP-Adig also colocalized with the ER at low expression levels (fig. S1F). To further define the localization of Adig in adipocytes, we fused Adig to APEX2, an enzyme that can be used to visualize proteins by electron microscopy (16). We transfected Adig-APEX2 into Adig knockout (KO; gene deletion) cells using adeno-associated viruses (AAVs) at levels on par with endogenous Adig levels (fig. S1G). We found a strong APEX2 signal on the ER (Fig. 1G). We then assessed the topology of Adig with a fluorescence-based protease protection assay in digitonin-treated cells (17). The EGFP from EGFP-Adig, but not from Adig-EGFP, was protected from digestion by protease K (Fig. 1H and fig. S1H), indicating that the N terminus of Adig is either embedded inside the bilayer or located within the ER lumen. Thus, Adig is a single-pass ER protein with a cytosolic C-terminal tail (Fig. 1I).

Adig interacts with and stabilizes seipin

Microproteins typically form a complex with larger proteins to modify their function (18, 19). To identify possible Adig partner(s), we overexpressed Adig-FLAG (or EGFP as a control) in mouse adipocytes with

¹Touchstone Diabetes Center, University of Texas Southwestern Medical Center, Dallas, TX, USA. ²Department of Anatomy and Stem Cells and Metabolism Research Program, University of Helsinki, Helsinki, Finland. ³Minerva Foundation Institute for Medical Research, Helsinki, Finland. ⁴Department of Physics, University of Helsinki, Helsinki, Finland. ⁵Department of Cell Biology, University of Texas Southwestern Medical Center, Dallas, TX, USA. ⁶Department of Health Sciences, Magna Graecia University of Catanzaro, Catanzaro, Italy. ⁷Department of Metabolic Medicine and Department of Adipose Management, Osaka University Graduate School of Medicine, Suita, Osaka, Japan. ⁸Synthetic and Systems Biology Unit, Biological Research Centre, Szeged, Hungary. ⁹Department of Biological Sciences, School of Life Sciences, Ulsan National Institute of Science and Technology, Ulsan, South Korea. ¹⁰Division of Metabolic Health and Disease, Oregon National Primate Research Center, Beaverton, OR, USA. ¹¹Department of Biophysics, University of Texas Southwestern Medical Center, Dallas, TX, USA. ¹²Center for Hypothalamic Research, Department of Internal Medicine, University of Texas Southwestern Medical Center, Dallas, TX, USA. ¹³Specialty Ophthalmology Discovery, Janssen R&D, Spring House, PA, USA. ¹⁴Sam and Ann Barshop Institute for Longevity and Aging Studies, Division of Endocrinology, Department of Medicine, University of Texas Health Science Center at San Antonio, San Antonio, TX, USA. ¹⁵Department of Diabetes and Cancer Metabolism, Beckman Research Institute, City of Hope National Medical Center, Duarte, CA, USA. ¹⁶Division of Cardiology, Department of Internal Medicine, University of Texas Southwestern Medical Center, Dallas, TX, USA. ¹⁷Department of Pharmacology, University of Texas Southwestern Medical Center, Dallas, TX, USA. ¹⁸Department of Biochemistry, University of Texas Southwestern Medical Center, Dallas, TX, USA. *Corresponding author. Email: philipp.scherer@utsouthwestern.edu (P.E.S.); elina.ikonen@helsinki.fi (E.I.) †These authors contributed equally to this work. ‡These authors contributed equally to this work.

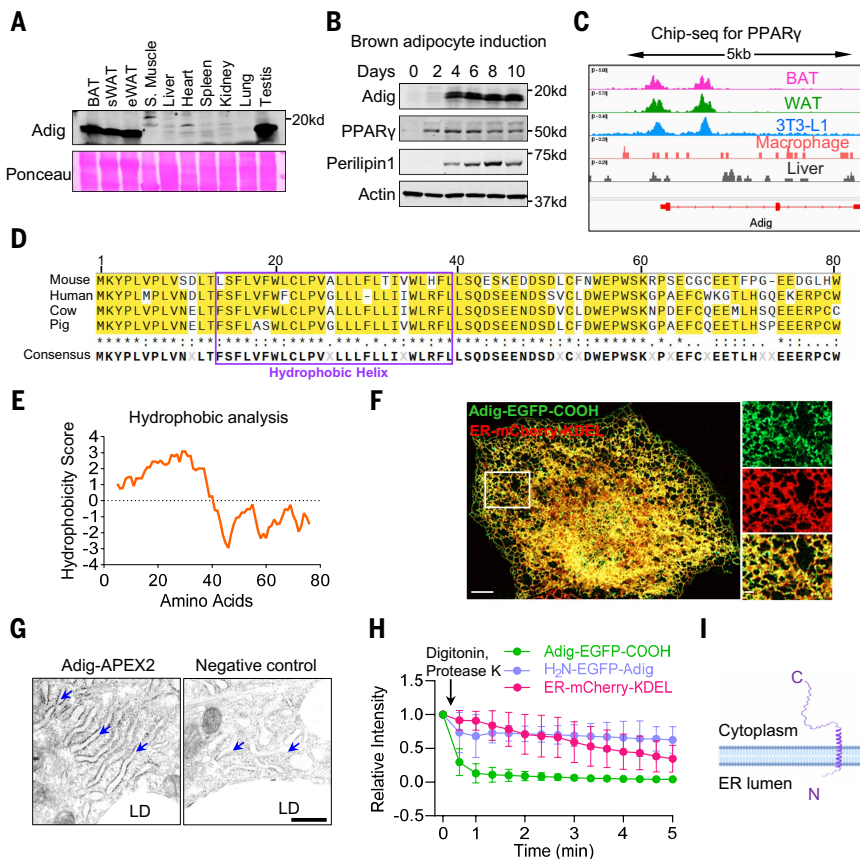


Fig. 1. Adipogenin is highly expressed in adipocytes and localized to the ER. (A) Immunoblot showing the protein expression profile of Adig in different mouse tissues. Adig protein is enriched in adipose tissues and in testis. S. muscle, skeletal muscle. (B) Immunoblot showing that Adig is strongly up-regulated during the adipogenesis of brown adipocytes in vitro. Preadipocytes were isolated from mouse BAT. (C) PPAR γ binding peak in the Adig promoter region and intron 1, as revealed in the Integrative Genomics Viewer. (D) Amino acid sequence alignment of Adig across different mammalian species. The putative α -helix sequence is highlighted with a purple box. (E) Hydrophobicity analysis of the amino acid sequence of mouse Adig. Scores were generated by Expsy ProtScale. (F) Immunofluorescence image showing that Adig colocalizes with the ER marker KDEL. Plasmids Adig-EGFP(C) and ER-mCherry-KDEL were transfected into HeLa cells. Scale bars are 5 μ m in the whole cell and 1 μ m in the inset. (G) Representative transmission electron microscopy images for Adig-APEX2 staining in the adipocytes. Preadipocytes were isolated from WAT in Adig flox mice and differentiated into mature adipocytes. To ensure that Adig-APEX2 is expressed at physiological levels, preadipocytes were transduced with AAV-iCre and AAV-Adig-Apex2. For the negative-control group, preadipocytes were transduced with AAV-EGFP or AAV-iCre. Scale bar is 500 nm. Blue arrows indicate the ER. (H) Adig topology analysis in HeLa cells. Adig-EGFP(C) or EGFP(N)-Adig plasmids were transfected into HeLa cells. A low concentration of digitonin was added to permeabilize the plasma membrane without disrupting the ER structure. Proteinase K was used to selectively cleave the cytosolically accessible parts of proteins without affecting portions hidden in the lumen of the organelles. Fluorescence was recorded in time-lapse mode. (I) Scheme for Adig localization, topology, and its putative structure. Data are presented as mean \pm SD in (H). Single-letter abbreviations for the amino acid residues are as follows: A, Ala; C, Cys; D, Asp; E, Glu; F, Phe; G, Gly; H, His; I, Ile; K, Lys; L, Leu; M, Met; N, Asn; P, Pro; Q, Gln; R, Arg; S, Ser; T, Thr; V, Val; W, Trp; and Y, Tyr.

AAVs, pulled down proteins with an anti-FLAG antibody, and analyzed them by mass spectrometry (Fig. 2A and fig. S2A). The most enriched protein with substantial sequence coverage was seipin (Fig. 2B). In addition, lipid droplet assembly factor 1 (LDAF1), which displays a strong interaction with seipin (20, 21), was also enriched in the Adig pull-downs (Fig. 2B and table S1).

Seipin exists as oligomers, and the seipin complex can be separated by size exclusion chromatography (gel filtration) (13, 22, 23). To explore the physical interactions between Adig and seipin oligomers, we transfected human embryonic kidney (HEK) 293T cells with Adig-FLAG alone or with seipin-Myc and Adig-FLAG and applied the cell lysates to

a gel filtration column. We analyzed the distribution of seipin and Adig in all fractions using immunoblotting. Adig, when expressed alone, migrated in fractions containing medium-molecular weight proteins, suggesting that Adig may form oligomers or it may interact with detergent micelles (Fig. 2, C and D). However, when Adig and seipin were coexpressed, they coeluted in the high-molecular weight fractions 22 to 26 (Fig. 2, C and D), indicating that Adig may bind to the seipin complex. To directly examine the interactions between Adig and seipin, we performed immunoprecipitations for the fractions obtained by gel filtration (Fig. 2E). Seipin displayed strong interactions with Adig in all fractions, and Adig and seipin levels were positively correlated across fractions (Fig. 2F), reflecting that Adig may interact with seipin monomers as well as oligomers.

Notably, seipin-Adig cotransfection strongly increased the expression levels of both proteins compared with single transfections (Fig. 2G). To assess whether this effect was due to protein stability, we treated cells with cycloheximide to inhibit new protein synthesis (fig. S2B). In the absence of seipin, the expression of Adig sharply decreased (fig. S2C). Analogously, seipin expression tended to decrease when Adig was absent (fig. S2C), and both proteins remained at high levels when coexpressed. To further explore the effect of Adig on the expression of endogenous seipin, we used human A431 cells, in which endogenous seipin was tagged with green fluorescent protein (GFP) (12) and Adig was undetectable. We transfected Adig-FLAG into these cells and analyzed the fluorescence intensities based on GFP and FLAG staining. As the expression of Adig increased, the seipin fluorescence correspondingly increased (Fig. 2, H and I). Moreover, the fluorescence of seipin-GFP was quite stable in Adig-expressing cells after cycloheximide treatment (fig. S2, D and E). To avoid the interference of other mammalian proteins in the seipin-Adig association, we exogenously expressed mouse seipin and Adig in yeast. We inserted mouse seipin-mNeonGreen into the endogenous locus of yeast *Sei1* (*SEI1::msSeipin-mNG*), and Adig was expressed with a weak or a strong promoter. Seipin-mNeonGreen fluorescence and foci became increasingly stronger as more Adig was expressed (fig. S2, F and G). Thus, seipin and Adig intrinsically stabilize each other through direct interactions.

The cryo-EM structure of the seipin-Adig complex

The structures of seipin complexes from different species have been well characterized (13, 14, 22). The amino acid sequence of mouse seipin is almost identical to that of human seipin (fig. S3). As was previously done for the human seipin complex (14), we purified the mouse seipin complex upon seipin and Adig coexpression (fig. S4, A to C) and determined its structure using single-particle cryo-EM (table S2). The two-dimensional class averages revealed two toroidal oligomers for the seipin complex, consisting of undecamers and dodecamers (Fig. 3, A and B). After classification, 17,212 particles were used to reconstruct the map of the undecameric seipin complex, and 32,123 particles were included in the reconstruction of the dodecameric seipin complex density map (fig. S4D). The undecamer map was

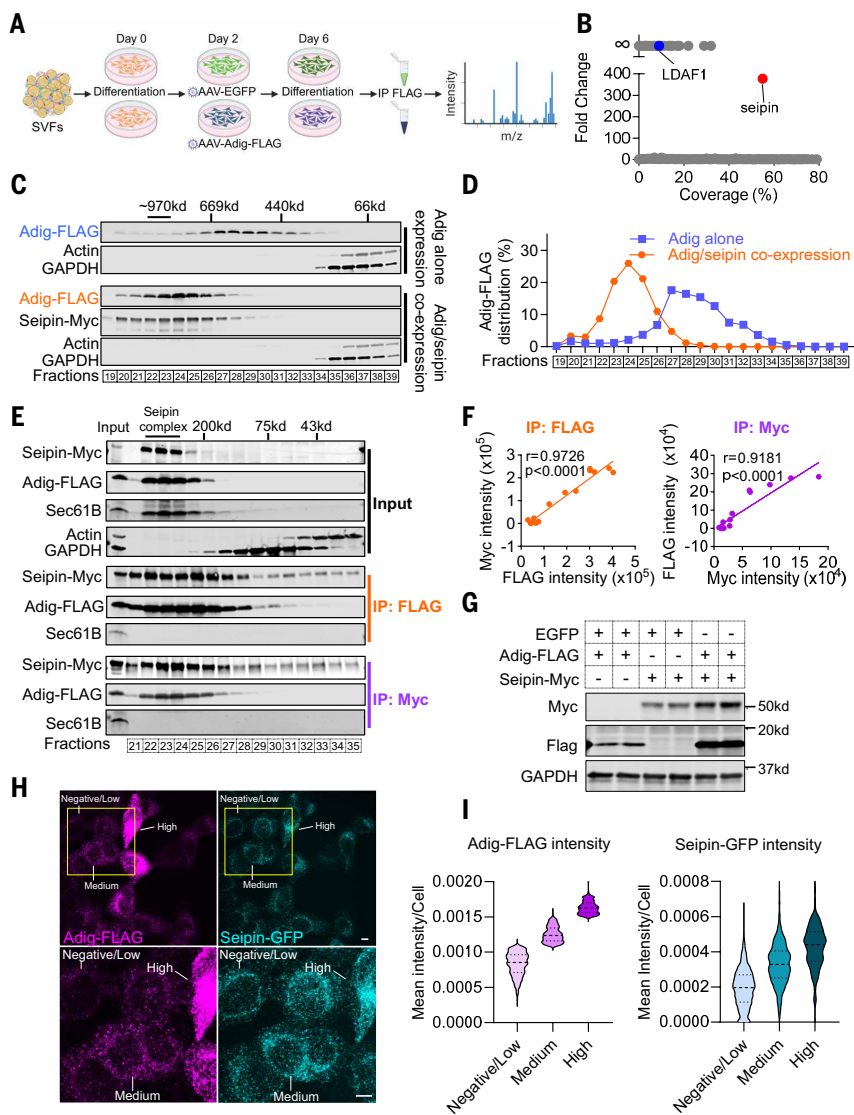


Fig. 2. Adig and seipin form a stable complex. (A) Workflow for identifying Adig-interacting proteins. The stromal vascular fractions (SVFs) were isolated from WAT and were transduced with AAV-EGFP or AAV-Adig-FLAG 2 days after the differentiation. IP, immunoprecipitation. (B) Analysis of all identified proteins pulled down by FLAG IP. Note that seipin was the most enriched protein with high sequence coverage. Proteins exclusively pulled down in the AAV-Adig-FLAG group were marked as “infinite.” (C) Gel filtration analysis for cell lysates from HEK293T cells with Adig-FLAG overexpression and seipin-V5/Adig-FLAG coexpression. A Superose 6 Increase column was used to fractionate the elution. GAPDH, glyceraldehyde phosphate dehydrogenase. (D) Distribution analysis for the Adig-FLAG expression in fractions from (C). Note that the peak of Adig-FLAG shifted from a lower-molecular weight fraction to the higher-molecular weight fractions in the presence of seipin-Myc. (E) IP analysis of the fractions from the gel filtration experiment. Seipin-Myc and Adig-FLAG were coexpressed in HEK293T cells, and then cell lysates were applied to a HiLoad Superdex-75 column. Note that the protein distributions differed from (C) because of the use of different columns. (F) Correlation analysis for the enriched seipin-Myc and Adig-FLAG proteins in the different fractions from (E). Significance was determined using a Pearson correlation coefficient test. (G) Immunoblot analysis for the expression of seipin-Myc and Adig-FLAG in HEK293A cells. The same amount of seipin-Myc or Adig-FLAG plasmids was transfected into the cells. (H) Representative fluorescence images of A431 cells expressing endogenously GFP-tagged seipin and Adig-FLAG. Cells with different expression levels of Adig-FLAG are indicated. Scale bars are 10 μ m. (I) Quantification of the mean fluorescence intensity of immunostained Adig-FLAG and seipin-GFP in cells exemplified in (H). Cells were divided into three groups based on their Adig-FLAG expression. The threshold intensity value is 0.0011 arbitrary units (a.u.) between Negative/Low and Medium and 0.0015 a.u. between Medium and High after an image-based background signal subtraction. The numbers of analyzed cells are as follows: Negative/Low, $n = 1676$; Medium, $n = 844$; and High, $n = 210$. The dashed line indicates the median; the dotted lines indicate quartiles.

similar to that of the purified human seipin complex (14), but with improved resolution (3.2 versus 3.8 Å) (fig. S5, A to C). The inner ring-like structure, corresponding to the luminal domain of seipin, was well resolved (Fig. 3C). However, only a small part of the TM segments was visible (Fig. 3C). The dodecamer appeared to be a more rigid structure with an overall resolution of 3.0 Å (fig. S5, D to F), with portions of the TM helices of seipin visible. In addition, extra TM densities were found, which could not be explained by seipin sequences (Fig. 3D). These densities appeared to be inserted between adjacent seipin monomers and were very likely contributed by the N terminus and hydrophobic helix of Adig (the C terminus was not visible) (Fig. 3D). Given the relatively low resolution in the TM regions, the side chains in these regions could not be confidently modeled (fig. S6A). However, this assignment of the TM helices agreed with the topology of Adig in the ER membrane (Fig. 1I) as well as the AlphaFold 3-predicted seipin-Adig complex (fig. S6, B and C), thereby reassuring the identity of these TM helices. Modeling of the luminal segment achieved high confidence in both the undecamer and dodecamer (fig. S6, D and E). In summary, we obtained two structures from the sample, the undecameric seipin complex (Fig. 3, C and E) and the dodecameric seipin-Adig complex (Fig. 3, D and F). Overall, the dodecameric seipin-Adig complex was more compact and featured a larger diameter with more hydrophobic residues embedded in the ER bilayer. In addition, the conformation of the seipin TM segments shared high similarity to those of the yeast counterpart despite the rather diverse amino acid sequence (13, 22) (fig. S7), highlighting their evolutionary conservation and functional importance.

Adig promotes the assembly of the seipin complex

The observation of mutual stabilization and the structure of the seipin-Adig dodecameric complex led us to hypothesize that Adig promotes or stabilizes the assembly of seipin complexes. We thus examined the assembly of newly synthesized seipin using seipin-degron-GFP expressing cells (24), in which the endogenous seipin can be depleted. We imaged cells at both the steady state and recovery stage (Fig. 4A). The number of newly formed seipin foci was significantly increased in Adig-positive cells compared with the adjacent Adig-negative cells (Fig. 4, B and C). When examining the involvement of Adig in the assembly of seipin complexes, we found that the endogenous seipin complexes manifested widespread colocalization with the Adig signal (Fig. 4D). The fraction of Adig-positive seipin foci was higher in the recovery stage than in the steady state (Fig. 4E), suggesting that Adig was actively participating in the assembly of newly translated seipin and that Adig could leave the seipin complex.

To assess how Adig affects the seipin complex assembly biochemically, we used gel filtration (23). When analyzing the elution of the wild-type (WT) protein and two natural variants [A212P (Ala²¹²→Pro) and L91P (Leu⁹¹→Pro)] of mammalian seipin expressed

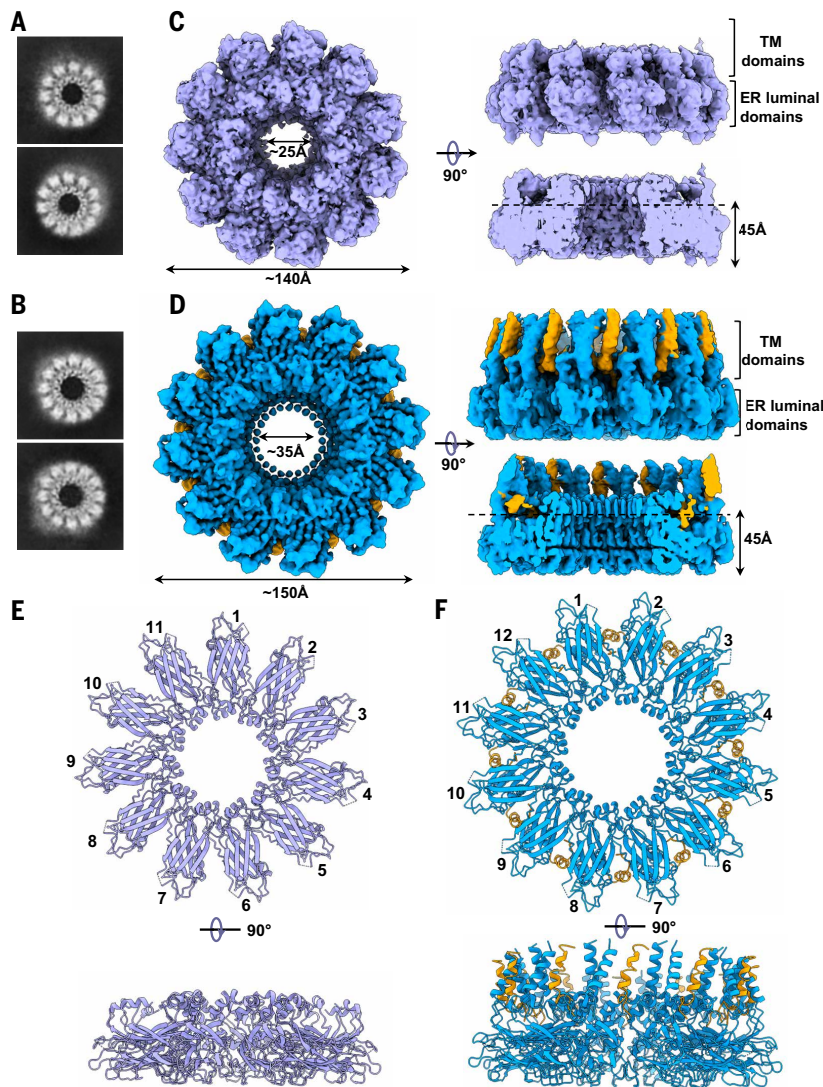


Fig. 3. Cryo-EM structure of the seipin-Adig complex. (A) Representative 2D class averages for the undecameric seipin complex. (B) Representative 2D class averages for the dodecameric seipin complex. (C) Cryo-EM density map for the seipin complex. Note that there is no obvious density for Adig. The top view reveals the 11 copies of the seipin subunits. The side view reveals the position of the TM and luminal domains in the seipin complex. A sliced view shows the cage-like structure. (D) Cryo-EM density map for the seipin-Adig complex. Adig had a separate density from seipin and is colored brown. The top view reveals the 12 copies of seipin-Adig subunits. The side view reveals the position of the TM and luminal domains in the seipin-Adig complex. The sliced view shows the cage-like structure. (E) Structural model of the undecameric seipin complex. The en face view is from the luminal side. (F) Structural model of the dodecameric seipin-Adig complex. The en face view is from the luminal side.

in HEK293T cells, we found that a fraction of WT seipin protein and most of the mutant seipin protein migrated as aggregates in fractions 18 to 21 (fig. S8, A and B), consistent with immunofluorescence staining (25–27). For comparison, the endogenous seipin in HeLa cells, validated by the disappearance of bands in the immunoblot upon sample boiling (28), migrated into fractions 22 to 25 (fig. S8B). As the relative Adig expression in HEK293T cells increased, the distribution of co-expressed seipin complexes shifted closer to that observed for endogenous seipin (Fig. 4F). Thus, when expressed with Adig, seipin appeared to form functional seipin-Adig complexes rather than seipin aggregates.

The TM segments of both seipin and Adig are involved in complex assembly

We sought to determine the structural basis for Adig's effect on seipin assembly in more detail. On a segmented map with three seipin and two Adig molecules, the first TM segment (TM1) of seipin and the TM2 from an adjacent seipin monomer provide a hydrophobic channel that specifically accommodated the α helix of Adig [(i) in Fig. 4G]. In addition, the N terminus of Adig appeared to be embedded within the seipin oligomer and laid close to the TMs of two neighboring seipin subunits [(iii) in Fig. 4G]. Moreover, the AlphaFold 3-based prediction (29), which provided potential structures of the segments that were not resolved by cryo-EM, manifested widespread interactions between seipin and Adig (fig. S6, B and C), further confirming the observations in our segmented map (Fig. 4G).

We then examined the contributions of different Adig and seipin domains on the stability and assembly of the seipin-Adig complexes by introducing mutations. For Adig, we introduced point mutations individually from amino acids 2 to 11. We replaced the TM in Adig with the one from FIT2 or deleted the C-terminal amino acids at positions 61 to 80 (fig. S9A). We also introduced point mutations into TM residues likely facing the same side (TM mutations 1 to 4; fig. S9B). We coexpressed these constructs with WT seipin and analyzed them for their stability and interactions with seipin using gel filtration. Conversely, we modified seipin constructs and expressed them with WT Adig. We truncated the N terminus (Δ NT), first transmembrane domain (Δ TM1), luminal domain (Δ LD), second TM domain (Δ TM2), and C terminus (Δ CT) of seipin (fig. S10A). We also swapped the seipin TMs with those from FIT2 (TMs replaced) and introduced point mutations in the switch region (GLR/FP 5A; fig. S10A), a region that plays a key role in LD formation (13). Together, our results (figs. S9 and S10) suggested that the interaction between seipin and Adig does not rely on a specific residue or isolated domain in either protein. Rather, seipin is almost completely intertwined with every segment in Adig, as suggested by the AlphaFold 3 prediction. The TM domains in seipin, visualized by cryo-EM, play a key role in integrating Adig into a seipin-Adig complex, and multiple domains of seipin, except for the luminal and C-terminal domains, stabilize Adig.

To investigate in further detail how Adig is involved in seipin oligomer assembly, we performed self-assembly coarse-grained molecular dynamics (MD) simulations using two seipin and two Adig monomers (Fig. 4H and movie S1). Adig frequently positioned itself between seipin monomers by interacting with their TM regions, although in one instance, seipin association occurred without Adig involvement. Based on these simulations, seipin dimer formation was ~9 times more likely with Adig than without it (Fig. 4H). The structural conformation of the Adig-associated seipin dimer aligned more closely with the cryo-EM-based model than the seipin-alone dimer (fig. S11A), as reflected by a lower root mean square deviation (fig. S11B).

In the cryo-EM structure, Adig binding improved the local resolution of all segments of the dodecameric seipin complex (fig. S5), suggesting an increased rigidity of the seipin complex. To test this, we performed atomistic MD simulations of the seipin-Adig dodecameric complex at a 1:1 stoichiometric ratio. We observed that the root mean square fluctuation for the seipin-Adig structure was lower than that

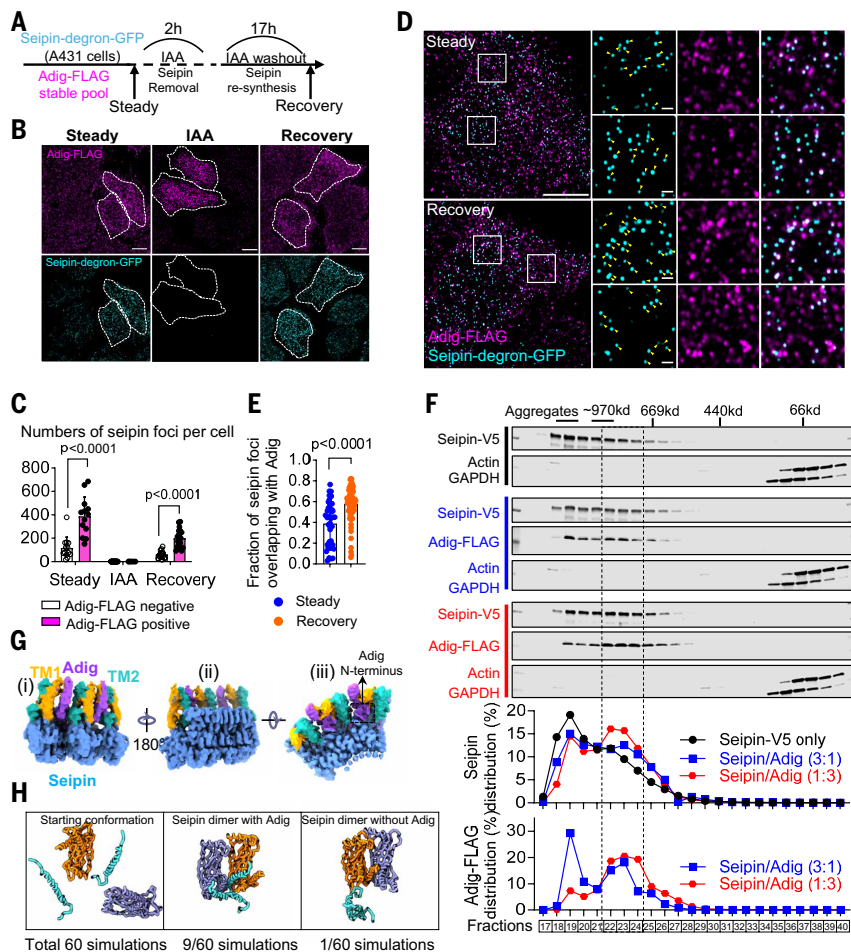


Fig. 4. Adig promotes the assembly and enhances the rigidity of seipin complexes. (A) Schematic showing the treatments of A431 cells with endogenous seipin-degron-GFP and Adig-FLAG expression. Seipin was degraded by 2 hours of indole-3-acetic acid (IAA) treatment. After IAA washout, seipin was resynthesized for 17 hours. (B) Airyscan fluorescence images of Adig-FLAG and seipin-GFP in the steady and recovery states and after IAA treatment. Adig-FLAG-expressing cells are highlighted with white dashed lines. Scale bars are 10 μ m. (C) Quantification of the number of seipin foci in cells with and without Adig-FLAG expression. $n = 13$ to 20 cells. Significance was determined using two-way analysis of variance (ANOVA) followed by Sidak's multiple comparison test. (D) Airyscan fluorescence images showing the overlap between Adig-FLAG and seipin-GFP in steady and recovery states. Yellow arrowheads indicate seipin foci overlapping with Adig. Scale bars are 10 μ m in the whole cell and 1 μ m in the insets. (E) Quantification of the fraction of seipin foci in contact with Adig foci. The numbers of analyzed cells are as follows: Steady, $n = 43$; and Recovery, $n = 83$ from two experiments. Significance was determined using an unpaired Student's t test. (F) Gel filtration analysis for cell lysates from HEK293T cells with seipin-V5 alone (black labels), seipin-V5/Adig-FLAG (3:1, blue labels) and seipin-V5/Adig-FLAG (1:3, red labels) overexpression. A Superose 6 Increase column was used to fractionate the lysates. Note that the distribution of seipin shifted from aggregate fractions to the native seipin complex fractions in the presence of Adig-FLAG. (G) Cryo-EM map of a local region including three copies of seipin and two copies of Adig. The two TM segments in seipin (TM1 and TM2) are colored brown and cyan. Adig is colored purple. Panel (i) shows the interactions between the Adig α helix and TM1/TM2. Panels (ii) and (iii) show the position of the N terminus of Adig. (H) Coarse-grained self-assembly simulations of two seipin and two Adig monomers. Ten out of 60 simulations resulted in seipin associating in the correct orientation. Of these 10 cases, an Adig monomer intercalated between two seipin monomers in nine cases. In only one case, seipin was assembled in the correct orientation without the participation of Adig. Data are presented as mean \pm SD in (C) and (E).

for the Adig-free seipin dodecameric structure, suggesting that Adig suppresses dynamic and thermal fluctuations, thereby stabilizing the seipin complex (fig. S11C). In addition, we explored the effect of Adig on the conformational symmetry of the inner lumen (hollow ring) of the seipin complex by measuring the luminal diameters $d1$ and $d2$

(fig. S11D). In the seipin-Adig complex, the values for both $d1$ and $d2$ converged to around 5.2 nm during the simulation (movie S2), indicating a circular lumen symmetry. By contrast, without Adig, $d1$ and $d2$ varied between 4.8 and 5.6 nm (movie S3), suggesting a deviation of the inner lumen from its regular circular symmetry (fig. S11E). These results support the view that Adig suppresses thermal fluctuations and increases the stability of the seipin complex.

Thus, Adig appears to act as a bridge to connect and stabilize the TM segments of two neighboring seipin subunits, thereby increasing the overall rigidity of the seipin complex. Through these interactions, Adig promotes the assembly of the dodecameric seipin complex (fig. S11F).

Adig affects the formation and growth of LDs

Because seipin is involved in multiple steps of LD biogenesis (11, 12, 24, 30), including triacylglycerol (TAG) nucleation, LD budding, LD growth, and LD protein targeting, we next explored the role of the seipin-Adig complex in these processes. We interrogated the process of seipin-mediated TAG nucleation by coarse-grained MD simulations (31, 32). To do this, we first considered the stoichiometry of seipin and Adig in the complex. Although the cryo-EM map exhibited 12 Adig subunits in the purified dodecameric seipin complex, the map assumed a C12 symmetry and calculated an average of thousands of particles (fig. S4). However, the complex might be heterogeneous with respect to seipin:Adig stoichiometry. Indeed, the fraction of colocalized seipin-Adig foci varied in the steady and recovery stages (Fig. 4E). Moreover, fluorescence recovery after photobleaching in live cells expressing seipin-mNeonGreen and Adig-mScarlet3 showed that the Adig signal, which colocalized with seipin, recovered to 50% in ~ 10 s after photobleaching (fig. S12, A and B). This suggests that Adig detaches from and reattaches to the seipin complex constantly. There may thus be several different types of seipin complexes: seipin-alone undecamers, seipin-alone dodecamers, Adig-poor seipin dodecamers, and Adig-rich seipin dodecamers (figs. S11F and S12C).

We then compared the ability of such seipin complex variants to concentrate TAGs. Simulations showed no substantial differences in TAG concentration between the undecameric seipin-alone complex, the dodecameric seipin-alone complex (movie S4), and the dodecameric Adig-poor seipin complex (12:2). However, the seipin complex with higher Adig content (12:4) slowed down the rate of TAG nucleation, and in the fully saturated seipin-Adig complex (12:12) (movie S5), TAG was completely blocked from migrating to the center of the seipin complex (Fig. 5A and fig. S13A). In agreement with the simulations, nascent LDs were associated with seipin complexes that lacked a visible Adig signal in A431 cells (Fig. 5B). In live cells, we tracked emerg-

ing LDs for a few seconds and found that they formed stable contacts with seipin complexes without Adig, whereas seipin-Adig complexes moved rapidly through their vicinity (fig. S13B).

To examine LD formation and growth, we imaged LDs in A431 cells at 20, 30, and 60 min after oleic acid (OA) treatment using LipidTox

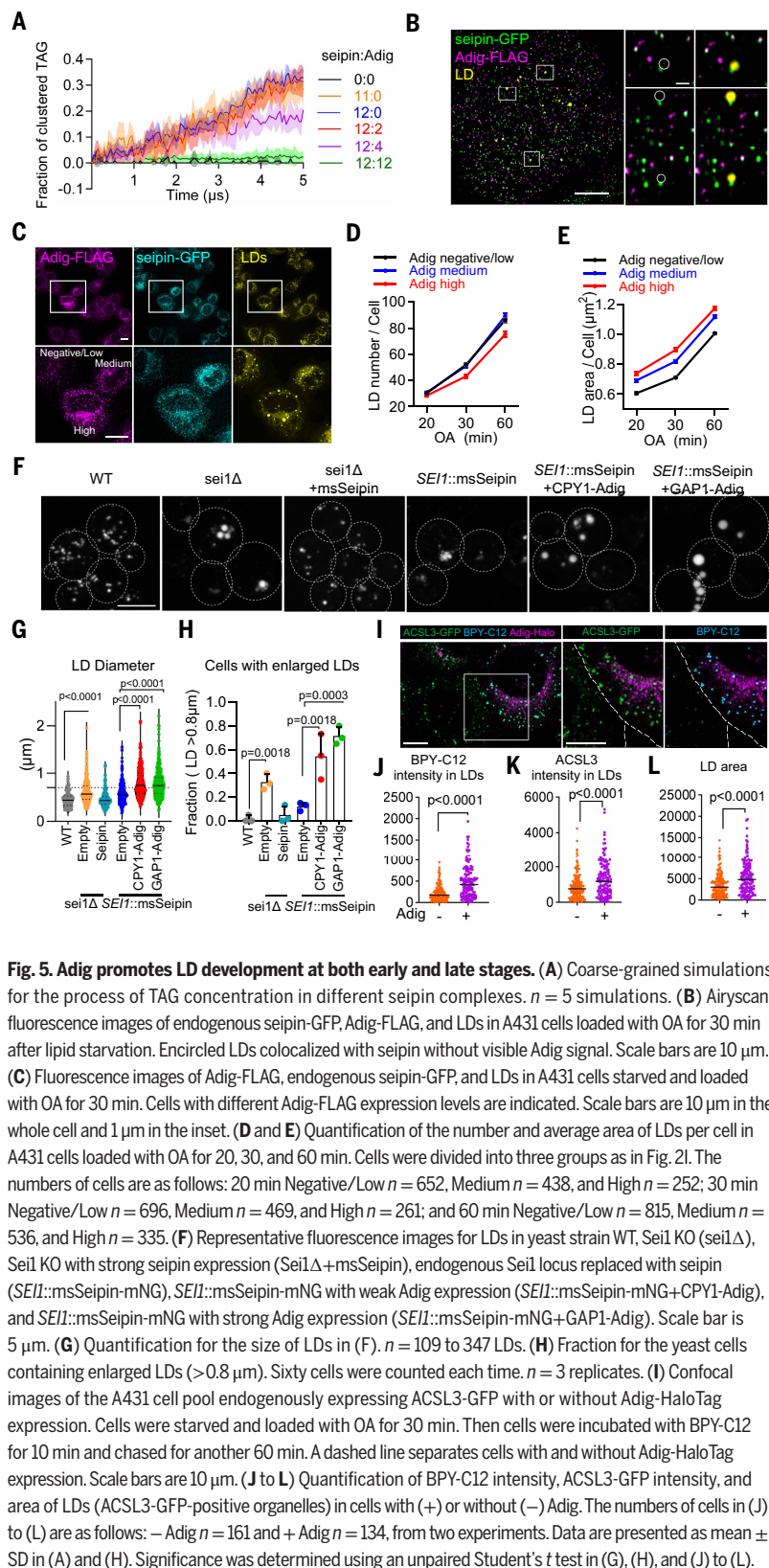


Fig. 5. Adig promotes LD development at both early and late stages. (A) Coarse-grained simulations for the process of TAG concentration in different seipin complexes. $n = 5$ simulations. (B) Airyscan fluorescence images of endogenous seipin-GFP, Adig-FLAG, and LDs in A431 cells loaded with OA for 30 min after lipid starvation. Encircled LDs colocalized with seipin without visible Adig signal. Scale bars are 10 μm . (C) Fluorescence images of Adig-FLAG, endogenous seipin-GFP, and LDs in A431 cells starved and loaded with OA for 30 min. Cells with different Adig-FLAG expression levels are indicated. Scale bars are 10 μm in the whole cell and 1 μm in the inset. (D and E) Quantification of the number and average area of LDs per cell in A431 cells loaded with OA for 20, 30, and 60 min. Cells were divided into three groups as in Fig. 2I. The numbers of cells are as follows: 20 min Negative/Low $n = 652$, Medium $n = 438$, and High $n = 252$; 30 min Negative/Low $n = 696$, Medium $n = 469$, and High $n = 261$; and 60 min Negative/Low $n = 815$, Medium $n = 536$, and High $n = 335$. (F) Representative fluorescence images for LDs in yeast strain WT, *Sei1* KO (*sei1* Δ), *Sei1* KO with strong seipin expression (*Sei1* Δ +*msSeipin*), endogenous *Sei1* locus replaced with seipin (*SEI1::msSeipin*-mNG), *SEI1::msSeipin*-mNG with weak Adig expression (*SEI1::msSeipin*-mNG+*CPY1-Adig*), and *SEI1::msSeipin*-mNG with strong Adig expression (*SEI1::msSeipin*-mNG+*GAP1-Adig*). Scale bar is 5 μm . (G) Quantification for the size of LDs in (F). $n = 109$ to 347 LDs. (H) Fraction for the yeast cells containing enlarged LDs (>0.8 μm). Sixty cells were counted each time. $n = 3$ replicates. (I) Confocal images of the A431 cell pool endogenously expressing ACSL3-GFP with or without Adig-HaloTag expression. Cells were starved and loaded with OA for 30 min. Then cells were incubated with BPY-C12 for 10 min and chased for another 60 min. A dashed line separates cells with and without Adig-HaloTag expression. Scale bars are 10 μm . (J to L) Quantification of BPY-C12 intensity, ACSL3-GFP intensity, and area of LDs (ACSL3-GFP-positive organelles) in cells with (+) or without (-) Adig. The numbers of cells in (J) to (L) are as follows: - Adig $n = 161$ and + Adig $n = 134$, from two experiments. Data are presented as mean \pm SD in (A) and (H). Significance was determined using an unpaired Student's *t* test in (G), (H), and (J) to (L).

(Fig. 5C and fig. S14, A and B). As the expression of Adig increased, the number of LDs decreased (Fig. 5D) but their size increased (Fig. 5E and fig. S14, C to E). Larger LDs were also observed upon Adig expression at 30 min after OA loading based on endogenous PLIN3 immunostaining (fig. S14F) (12, 33). Because a similar amount of TAG was

made in 60 min in the presence and absence of Adig (fig. S14G), the introduction of Adig seemed to modify the TAG distribution rather than its cellular level in A431 cells. Notably, the LD size distributions were unaffected when Adig was expressed in seipin KO cells (fig. S15), indicating that the effect of Adig on LDs is strictly dependent on the presence of seipin.

We also used yeast cells to assess the effect of seipin-Adig complexes on LDs. The endogenous *Sei1* was replaced with mouse seipin-mNeonGreen (*SEI1::msSeipin*-mNG) and Adig was expressed with either a weak or a strong promoter. As reported before (6), exogenous expression of seipin driven by a strong promoter rescued the LD abnormalities in yeast with *Sei1* deletion (*sei1* Δ + *msSeipin*). The less active endogenous seipin promoter did not complement *sei1* Δ with mouse seipin (*SEI1::msSeipin*) but did increase LD size with Adig expression (Fig. 5F). The size of LDs and fractions of cells containing enlarged LDs increased in an Adig dose-dependent manner (Fig. 5, G and H), whereas Adig had no effect on the morphology of LDs in WT yeast (fig. S16, A to C). We further assessed neutral lipid abundance in these yeast strains under normal growth conditions. Adig expression significantly increased the accumulation of TAGs and sterol esters in the presence of seipin-mNeonGreen (fig. S16, D and E). Thus, Adig enhances TAG synthesis as well as flux into LDs in yeast.

Previous reports indicated that the ER-to-LD relocation of LD-targeting proteins is regulated by seipin. However, the seipin complex exerts opposite effects on the relocation of early and late LD-targeting proteins by promoting the trafficking of early LD-targeting proteins (e.g., ACSL3) (20, 34) but repressing the relocation of late LD-targeting proteins (e.g., GPAT4) (35, 36). We asked whether seipin-Adig complexes influenced this process. A431 cells with endogenous ACSL3-GFP expression were transfected with Adig-HaloTag plasmid, and LDs were then induced with OA for 30 min, followed by labeling with BPY-C12 for 10 min. This approach enabled the simultaneous tracking of lipid flux and ACSL3 relocation (Fig. 5I) (12). The incorporation of BPY-C12 into nascent LDs, manifested by fluorescence intensity in LDs, was significantly enhanced (Fig. 5, I and J), suggesting increased TAG flux into LDs in Adig-expressing cells (fig. S16F). The presence of Adig also significantly increased the intensity of ACSL3-GFP on LDs and the area of LDs (Fig. 5, K and L), indicating more efficient ACSL3 relocation from the ER to LDs (fig. S16F).

We further examined the relocation of a late LD-targeting protein, GPAT4 (36). The presence of Adig significantly increased the fraction of cells with GPAT4-positive LDs (fig. S17). We then used gel filtration analysis to study whether Adig affected seipin-GPAT4 interaction. We reasoned that as seipin aggregates or complexes consistently migrated into fractions 18 to 28 (Fig. 4F), any protein interacting with seipin would likewise shift into these fractions. Indeed, the presence of seipin drove GPAT4 into fractions 18 to 23, with a corresponding reduction in free GPAT4 in fractions 30 to 39 (fig. S18A). These results are in line with previous data and confirm a strong interaction between seipin and GPAT4 (35, 37). When we coexpressed Adig, seipin, and GPAT4, seipin-Adig complexes migrated into fractions 23 to 25 with a small portion of GPAT4 (fig. S18A), whereas the free GPAT4 content in fractions 30 to 39 increased markedly (fig. S18B). As a negative control, we tested the ER protein AGPAT2, another enzyme in the TAG-synthesizing pathway. Seipin expression, either with or without Adig, had no effect on the AGPAT2

distribution in gel filtration (fig. S18, C and D). Thus, Adig modifies the seipin-GPAT4 interaction by enabling GPAT4 dissociation from the seipin complex, presumably facilitating its relocation to LDs (fig. S18E).

Overall, Adig expression accelerates TAG flux to emerging LDs and enhances the LD targeting of ACSL3 and GPAT4. This suggests a positive effect on the ER-to-LD relocation of both early and late LD-targeting proteins, thereby promoting lipid storage (figs. S16F and S18E).

Adig overexpression enhances adipose tissue expansion in mice

To probe the functional role of seipin-Adig complexes in adipose tissues, we established a transgenic mouse model in which Adig expression could be induced specifically in adipocytes in adult animals (Adig iTG) (fig. S19A). The Adig protein was increased substantially in adipose tissues from iTG mice fed a diet containing doxycycline (Dox) (fig. S19B). We next compared the abundance of the seipin-Adig complexes in adipose tissues from control and Adig iTG mice.

We first determined the distribution pattern of endogenous seipin and Adig in brown adipose tissue (BAT) during gel filtration, as the seipin-Adig complex consistently migrated into fractions 22 to 26 (Fig. 4F and fig. S9, E and F). Endogenous Adig protein in adipose tissues was highly enriched in these seipin complex-containing fractions 22 to 26 (fig. S19C). Because the seipin antibody was unable to recognize endogenous seipin protein in adipose tissues (fig. S19C), we subjected samples from fractions 23 to 25, 32, and 39 to mass spectrometry to determine the relative seipin and Adig abundance. Both seipin and Adig concentrated in fractions 23 to 25, but not in 32 or 39 (fig. S19D). Next, we compared the relative abundance of seipin complexes from control and Adig iTG mice. Similarly, the lysates from iTG BAT were applied to gel filtration (fig. S19E), and the proteins from fractions 23 to 25 were analyzed by mass spectrometry. Seipin abundance in fractions 23 and 24 increased (fig. S19F), implying enhanced stability and assembly of seipin complexes upon Adig overexpression. Thus, it seems that endogenous seipin primarily exists in a higher-order complex, and endogenous Adig forms a complex with seipin in adipose tissues.

In mice, body weights displayed a tendency to increase after Adig overexpression for 2 weeks (fig. S20A). Specifically, the weight of BAT, inguinal white adipose tissue (iWAT), and gonadal white adipose tissue (gWAT) increased significantly (Fig. 6A). The LDs in BAT and WAT from Adig iTG mice were enlarged (Fig. 6B). In line with this, the content of TAGs and cholesterol in BAT from iTG mice was elevated (Fig. 6C). We further determined the TAG profiles in BAT by lipidomics. Almost all of the TAG species detected were increased upon Adig overexpression (Fig. 6D), with no specific TAGs disproportionately enriched in Adig iTG mice compared with controls (fig. S20B). A TAG clearance test revealed that Adig overexpression increased the TAG uptake from circulation (fig. S20C). We also monitored the long-term effects of Adig overexpression in adipose tissues. The body weights of the Adig iTG mice increased (fig. S21A). Notably, the visible BAT in iTG mice shrank (fig. S21B), likely due to a conversion of BAT into WAT. The residual brown adipocytes in the Adig iTG mice displayed highly enlarged LDs (fig. S21C). Furthermore, long-term Adig overexpression increased the weights of iWAT and gWAT, and both fat pads displayed cells with enlarged LDs (fig. S21, D to G).

To confirm that the impact of Adig on adipose tissues depends on the expression of seipin, we crossed the Adig iTG mice with adipocyte-specific seipin knockout (conditional knockout, cKO) mice (38) to generate the Adig iTG

with seipin cKO mice (iTG/cKO) (fig. S22A). After feeding the mice a Dox-containing diet for 4 days, we evaluated LD morphology in different adipose tissue depots. As expected (38, 39), the seipin cKO significantly decreased fat mass in BAT, iWAT, and gWAT. Although Adig overexpression increased the fat mass in control mice, it had no effect on the expansion of the adipose tissues in seipin cKO mice (fig. S22, B to D). The seipin deletion led to the formation of some enlarged LDs, which were interspersed in the BAT. Moreover, visible LDs were completely absent in some brown adipocytes in seipin cKO and iTG/cKO mice, contrary to the widespread enlargement of LDs in the Adig iTG mice (fig. S22E). In WAT, seipin deletion led to the accumulation of interstitial tissue, with dispersed adipocytes containing enlarged LDs. By contrast, the WAT in Adig iTG mice did not display abnormalities, except for crowded and enlarged LDs (fig. S22, F and G).

Thus, Adig overexpression in mouse adipose tissues led to enlarged LDs and enhanced TAG accumulation. This process depends on the presence of seipin in adipose tissues.

Adig deletion decreases TAG incorporation into adipose tissues

To gain insight into the function of endogenous Adig in adipose tissues, we conducted Adig loss-of-function studies in mice. We established a mouse model in which Adig can be eliminated from adipocytes in a Dox-inducible manner. To this end, we first generated Adig flox mice (Adig^{fl/fl}) (fig. S23A) and crossed them with adiponectin-rtTA/TRE-Cre mice to get inducible adipocyte-specific Adig KO mice (Adig iAKO) (fig. S23B). To avoid the potential effects of Adig removal on adipogenesis, we induced the Adig deletion at 5 to 6 weeks of age when

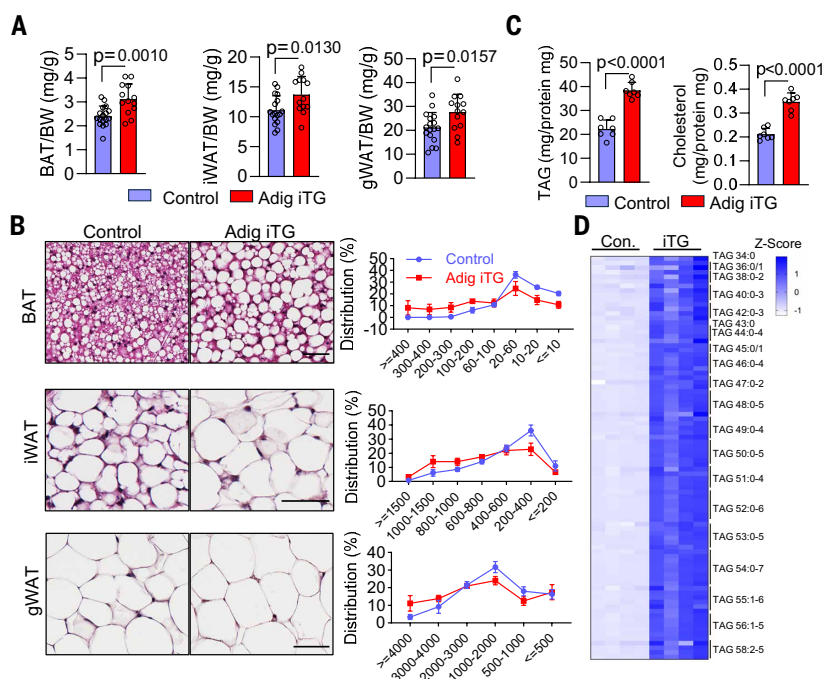


Fig. 6. Adig overexpression increases TAG accumulation in LDs. (A) Adig overexpression increased the mass of BAT, iWAT, and gWAT. $n = 13$ to 17 mice. (B) Hematoxylin and eosin (H&E) images showing that Adig overexpression increases the size of LDs in BAT, iWAT, and gWAT. For BAT, $n = 6$ replicates. For each replicate, 1161 to 5600 LDs were separated into eight groups according to their size. For iWAT, $n = 6$ or 7 replicates. For each replicate, 214 to 318 adipocytes were separated into seven groups according to their size. For gWAT, $n = 7$ or 8 replicates. For each replicate, 346 to 587 adipocytes were separated into six groups according to their size. Scale bars are 50 μm . (C) Adig overexpression increased the TAG and cholesterol content in BAT. $n = 7$ mice. (D) Heat map showing lipidomic profiling for the TAGs isolated from BAT in control and iTG mice. The amount of TAGs was normalized to total protein, then standardized with a Z score. $n = 4$ replicates. Data are presented as mean \pm SD. Significance was determined using an unpaired Student's t test in (A) and (C).

the adipose tissues are already well developed. Four weeks after exposure to a Dox-containing diet, the Adig protein was completely removed from BAT and WAT (Fig. 7A). The body weights of the iAKO mice were comparable to those of the control mice (fig. S23C). To compare the presence of the seipin complex in BAT from Adig^{f/f} and iAKO mice, cell lysates from BAT were fractionated by gel filtration and analyzed by mass spectrometry (fig. S23D), as described above. The

seipin complexes in fractions 24 and 25 were decreased by ~75% in BAT lysates from iAKO mice (Fig. 7B).

LDs in the BAT of iAKO mice were much smaller than the ones in Adig^{f/f} mice, although we observed several enlarged LDs (Fig. 7C). The accumulation of different species of TAG was substantially decreased in BAT from iAKO mice (Fig. 7D). To explore the fatty acid uptake in adipose tissues, we injected [³H]-triolein into mouse arteries, collected blood at various time points, and subsequently harvested different tissues. iAKO mice manifested delayed clearance of [³H]-triolein (Fig. 7E), in agreement with impaired overall TAG clearance in iAKO mice (fig. S24A). Furthermore, TAG uptake of BAT in iAKO mice was severely reduced (Fig. 7F), whereas no significant differences were observed in the uptake into iWAT and gWAT, liver, heart, and skeletal muscle (fig. S24, B to F).

Seipin deletion impairs the differentiation of white, but not brown, adipocytes in vitro (38, 40). We examined whether endogenous Adig forms a complex with seipin in differentiated adipocytes and whether Adig affects adipogenic differentiation. In gel filtration experiments, almost all Adig migrated into seipin complex-containing fractions 22 to 26, distinct from the Adig-alone distribution in HeLa cells (Fig. 7G). A faint band in these fractions was recognized by the seipin antibody, presumably representing the endogenous seipin because it aggregates after boiling (28) (Fig. 7G). To validate these results, we determined the abundance of seipin and Adig in fractions 24 and 25 (fig. S25A), confirming that the endogenous Adig bound to the seipin complex in differentiated adipocytes just as it does in adipose tissues.

To examine whether these seipin-Adig complexes contributed to the differentiation of adipocytes, we expressed iCre in both brown and white adipocyte precursors isolated from Adig^{f/f} mice and induced them to undergo adipogenesis. This approach achieved efficient Adig elimination (fig. S25B), accompanied by impaired adipogenesis of white adipocytes (fig. S25C). In the few apparent adipocytes, the total LD area decreased significantly upon Adig deletion (fig. S25D). By contrast, Adig removal had no apparent effect on adipogenic differentiation of brown adipocytes (Fig. 7H). However, the loss of Adig decreased the total area of LDs in individual cells (Fig. 7I), consistent with the decreased lipid content in differentiated brown adipocytes lacking seipin (38).

To summarize, Adig deletion impaired the assembly of seipin complexes in adipocytes. Consequently, TAG uptake and deposition decreased upon Adig deletion.

Discussion

Previous MD simulations have revealed that the TM segments of seipin play a crucial role in attracting TAG and promoting LD budding (30–32). However, owing to the lack of details in the atomic structure of the TM segments in previous reports, concerns have been raised about the accuracy of these simulations. Recently, two studies of the

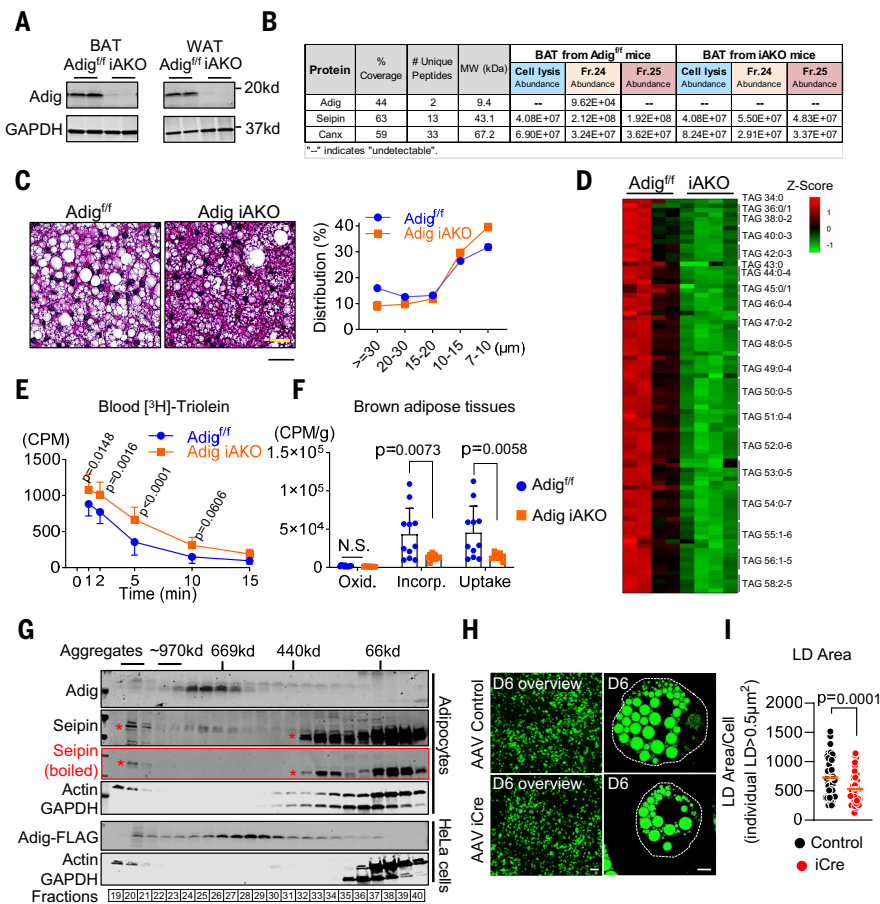


Fig. 7. Adig deletion decreases TAG incorporation into adipose tissues. (A) Validation of the Adig KO in adipose tissues. Mice were fed with Dox-containing diet for 4 weeks. (B) Quantification of seipin abundance in whole-cell lysates and in fractions 24 and 25. The whole-cell lysate was extracted from BAT. Then the same amount and volume of protein was applied to a Superose 6 Increase column. Protein abundance was determined by mass spectrometry. ER protein Canx was used as an internal control. (C) Adig elimination decreases the LD size in BAT. Representative hematoxylin and eosin (H&E) staining is shown. $n = 4$ replicates. For each replicate, 2933 to 10,242 LDs were separated into five groups according to their size. Scale bar is 20 μm . (D) Heat map showing lipidomic profiling for the TAGs isolated from BAT. TAG abundance was normalized to the total protein amount first, then standardized with a Z score. $n = 4$ replicates. (E) Adig deletion impairs the clearance of [³H]-triolein from circulation. Equivalent amounts of [³H]-triolein were injected into the circulation. Then, 1, 2, 5, 10, and 15 min after injection, blood was collected for radioactive measurement. $n = 10$ or 11 mice. CPM, counts per minute. (F) Adig iAKO decreases the uptake of [³H]-derived fatty acids in BAT. Oxi., oxidized fatty acids; Incomp., fatty acids incorporated into lipids; Uptake, total amount of absorbed fatty acid (oxidized and incorporated). $n = 9$ to 11 mice. (G) Gel filtration analysis of cell lysates from differentiated brown adipocytes and Adig-expressing HeLa cells. Note that the endogenous seipin band disappeared upon boiling the sample. The red asterisks indicate the nonspecific bands. (H) Fluorescence images showing that Adig deletion has no impact on the differentiation of brown adipocytes but does reduce LD growth. Pre-adipocytes were isolated from BAT of Adig^{f/f} mice and transduced with control and iCre AAVs. Six days after adipogenic induction (D6), cells were stained with BODIPY. Scale bars are 100 μm (left) and 10 μm (right). (I) Adig deletion in brown adipocytes decreases total LD areas per cell. $n = 63$ to 66 cells. Only LDs with an area $> 0.5 \mu\text{m}^2$ were considered. Data are presented as mean \pm SD. Significance was determined in (E) and (F) using a two-way ANOVA followed by Sidak's multiple comparison test and in (I) using an unpaired Student's t test in (I).

yeast seipin ortholog Sei1 successfully resolved the TM structure (13, 22). One study proposes a conformational switch model in which the TMs explain the process of TAG nucleation, LD budding, and LD growth (13). However, given the sequence diversity, the yeast TM structure may not reflect the structure of human seipin. Moreover, the conformational switch model is incompatible with our present understanding of the human seipin complex as an undecamer. Our study may pave the way to solving these issues. First, with the addition of Adig to the seipin complex, the TM segments were stabilized and captured by cryo-EM, which gave us the opportunity to include TM segments in MD simulations. Second, our data suggest that seipin-Adig complexes (of unknown stoichiometry) may be associated with LDAF1. They likely assemble into a dodecameric seipin complex, which presumably is more rigid and structurally resolvable than the seipin-LDAF1 undecameric complex. The stabilized seipin structure may allow the resolution of the lipid droplet assembly complex, consisting of seipin and LDAF1/Promethin (20, 21).

The cryo-EM structures and AlphaFold 3 models of the seipin-Adig complex indicate that at least two segments in Adig mediate the interaction with seipin. These interactions may largely facilitate the assembly and enhance the stability of the overall seipin structure. Notably, in MD simulations, the presence of Adig facilitated the formation of a seipin dimer, suggesting a distinctive role for Adig in the assembly of higher-order seipin complexes. Additionally, Adig appeared to alleviate the formation of seipin aggregates, highlighting its importance for seipin folding. Based on these observations, we propose that Adig acts as a structural chaperone for seipin complexes: Seipin and Adig may interact with each other shortly after translation and then assemble into an Adig-rich seipin dodecameric complex; individual Adig monomers may later dissociate from the complex, resulting in a stoichiometric heterogeneity of seipin-Adig complexes. We propose that through modulating Adig association, the function of the seipin complexes can be regulated. Further work is needed to evaluate whether this can be used as a strategy to alleviate seipin-related diseases.

It is technically challenging to distinguish the functions of the seipin-Adig complexes with different stoichiometries. However, according to MD simulations and imaging of nascent LDs, it is likely that only the seipin-alone or Adig-poor seipin complexes mediate TAG nucleation and LD budding. These findings imply that Adig is not directly required for LD formation—a process that occurs in most cells that lack Adig expression—but instead indirectly regulates this process. The Adig-rich seipin complexes may block TAG entry, leading to a more efficient channeling of TAG into a limited number of seipin (alone or Adig-poor) complexes and consequently faster growth of fewer LDs. Mechanistically, with Adig enrichment in the complex, seipin TM segments may be too rigid to execute conformational changes during TAG nucleation and LD budding (41).

Two LD-targeting proteins, ACSL3 and GPAT4, were enriched on LDs in Adig-expressing cells. The rapid ACSL3 relocation may be a secondary effect of efficient TAG shunting to fewer LDs in Adig-expressing cells, because LD formation is a self-reinforcing stepwise process (33). It is also possible that excess seipin complexes, induced by Adig expression, provide extra contacts between nascent LDs and the ER, thereby facilitating the relocation of early LD-targeting proteins (12, 42). Conversely, the Adig-induced replacement of GPAT4 from seipin complexes may facilitate its relocation to expanding LDs. Moreover, during LD expansion, it is likely that the elevated TAG-synthesizing pathway plays a role, because TAG accumulation significantly increased upon Adig expression in adipocytes and yeast. Previous reports have shown that seipin may associate with GPAT3/4 (35) and LPIN1 (43) in mammalian cells, and with Nem1, Lro1, and Yft2 in yeast (44), to fine-tune LD formation. Further investigation of the relationship between varying seipin-Adig complexes and TAG-synthesizing enzymes may elucidate the molecular details of Adig-induced LD expansion.

In the physiological context, endogenous Adig in adipocytes or steatotic hepatocytes likely functions to maintain a pool of preassembled seipin-alone or seipin-Adig complexes, poised to facilitate LD formation and expansion. This reservoir appears to be essential for the rapid uptake of TAG in some conditions (e.g., the postprandial state). The transcription, translation, and assembly of higher-order seipin complexes is a time-intensive process, whereas LD biogenesis must occur almost instantly upon lipid influx. By maintaining a preassembled standby state, seipin-Adig complexes may help cells to initiate LD formation and growth as soon as lipids are absorbed.

Materials and methods

Cell culture and transfection

HeLa (ATCC, no. CCL-2) and HEK293T (ATCC, no. CRL-3216) were cultured in DMEM (Thermo Fisher Scientific, no. 11995-065) with 10% FBS (GeminiBio, no. 100-106) and 1% penicillin/streptomycin (Sigma, no. P4458). A431 (ATCC, no. CRL-1555) (24) were cultured in DMEM (Gibco, no. 21969) with 10% FBS (Gibco, no. A5256701), 2 mM GlutaMAX (Gibco, no. 35050-038), and penicillin/streptomycin (100 U/ml each, Gibco, no. 15140-122) at 37°C with 5% CO₂. Cells were transfected at 50-70% confluency using PEI (linear, MW 25000; Polysciences, no. 23966-1) with Opti-MEM (Thermo Fisher Scientific, no. 31985070). Typically, 1.0 µg plasmid was mixed with 3.0 µl of PEI for a well of 12-well plates.

For mouse Adig-FLAG expression in A431 seipin-degron-GFP cells (45), cells were transfected with pcDNA3.1-Aig-FLAG using Lipofectamine LTX (Thermo Fisher Scientific, no. 15338083). A pool of Adig-FLAG-expressing seipin-degron cells was selected 24 hours after transfection by 0.8 mg/ml geneticin G418 sulfate (Gibco, no. 11811-031) treatment for 7 days. Wild-type A431 cells, A431 cells with endogenous ACSL3-GFP expression (12), A431 seipin knockout (KO) cells [S2AB-15 clone in (12)], and A431 seipin-degron-GFP cells were transfected with pPGK-Adig-FLAG-mScarlet3 or Adig-FLAG-HaloTag plasmids as described above. The Adig-positive cells were enriched by FACS.

In seipin recovery experiments, cells were treated with 0.5 mM IAA (Santa Cruz, no. 215171) for 2 hours to degrade seipin. Then IAA was washed out with PBS, and cells were cultured in normal growth medium for 17 hours to allow seipin re-synthesis. In seipin-GFP stability experiments, cells were treated with 1 µg/ml cycloheximide (Sigma-Aldrich, no. C7698) for the indicated times.

Brown and white adipocytes were differentiated *in vitro*, as previously described (46, 47). Stromal vascular fractions were isolated from brown or subcutaneous adipose tissues by collagenase digestion and cultured in DMEM/F12 medium containing GlutaMAX (Thermo Fisher Scientific, no. 15750060) with 10% FBS and 1% penicillin/streptomycin at 37°C with 10% CO₂. For white adipocytes, induction was performed at full confluency. A cocktail containing 0.5 mM 3-isobutyl-1-methylxanthine (IBMX), 1 µM dexamethasone, 5 µg/ml insulin and 1 µM rosiglitazone was added to the medium to initiate the differentiation. Forty-eight hours later, the induction medium was replaced with maintenance medium (5 µg/ml insulin in culture medium). For brown adipocytes, the induction medium contains 0.5 mM IBMX, 1 µM dexamethasone, 5 µg/ml insulin. Similarly, after 48 hours, the induction medium was replaced with maintenance medium (5 µg/ml insulin, 30 µM T3).

Cell staining, light microscopy, and image analysis

To examine the expression of Adig and seipin-GFP, A431 cells were seeded on fibronectin-coated (10 µg/ml, Roche, no. 11080938001) LabTEK II chambers (Thermo Fisher, no. 155409) for Airyscan imaging or 384-well imaging plates (Corning, no. 4518) for confocal high-content imaging. Before staining, the cells were fixed with 4% PFA for 20 min in a buffer containing 250 mM HEPES (pH 7.4), 100 µM CaCl₂, and 100 µM MgCl₂. To stain Adig-FLAG, cells were first quenched in 50 mM NH₄Cl for 10 min, and washed with PBS, and then permeabilized in 0.1% Triton X-100 in PBS for 10 min. The cells were blocked

for 1 hour in blocking solution (1% BSA and 0.1% Tween-20 in PBS). Subsequently, cells were incubated in blocking solution containing anti-FLAG primary antibody (Sigma-Aldrich, no. F1804, 1:1000) for 1 hour in 37°C, washed with PBS, and incubated in blocking solution containing Alexa Fluor 647-conjugated anti-mouse secondary antibody (Thermo Fisher Scientific, no. A31571, 1:200) for 1 hour in RT. After immunostaining cells were stained with DAPI (5 µg/ml, Sigma-Aldrich, D9542) in PBS for 10 min, washed with PBS and imaged in PBS.

To analyze lipid droplet formation, cells were seeded on LabTEK II chambers (Airyscan imaging) or 384-well imaging plates (Opera Phenix imaging) and stringently delipidated for 18 hours, as described previously (48). After delipidation, cells were washed twice with PBS, loaded with 200 µM oleic acid [OA, Sigma-Aldrich, no. O1008, complexed with BSA as described before (49)] in 5% lipoprotein deficient serum [LPDS, made from FBS as previously described (50)]-containing serum-free medium for the indicated times, then fixed and stained as above. To detect lipid droplets, HCS LipidTOX red (Thermo Fisher Scientific, no. H34476, 1:5000 in PBS) or HCS LipidTOX Deep Red (Thermo Fisher Scientific, no. H34477, 1:5000 in PBS) was added to the cells 30 min before imaging.

Cells were imaged with a Zeiss LSM 880 confocal microscope and Airyscan processed or with a Perkin-Elmer Opera Phenix high-content imaging system, as described before (48). To quantify the number of seipin foci and seipin overlap with Adig-FLAG in Airyscan images, cells were manually segmented, and seipin and Adig signals were segmented by using Ilastik (51) and CellProfiler (52) with a custom module (12). The fraction of seipin foci overlapping with Adig was calculated by dividing the number of seipin spots overlapping with Adig spots by the number of all seipin spots per cell. In high-content imaging of seipin-GFP, Adig-FLAG, and lipid droplet formation, Z-stacks were acquired to span whole cells, and image stacks were maximum intensity projected with custom MATLAB (2019b) scripts. The nuclei were segmented on DAPI channel with the generic-nucleus segmentation model of Biological Image Analysis Software (BIAS) Lite (Single-Cell Technologies Ltd. V1.1.0) and cells were segmented with CellProfiler (MATLAB 2019b) (49). Lipid droplets were identified with Ilastik (51) and segmented in CellProfiler with a custom module (24) based on Ilastik's probability map. Adig-FLAG-expressing A431 cells were divided into three categories as described in Fig. 2H in R (version 4.4.0). Lipid droplet analysis on Airyscan images of seipin knockout cells with and without Adig was done as described above and mean intensity of 0.002 a.u. on Adig-mScarlet3-channel was used as a threshold for classifying cells as Adig-negative and Adig-positive. In high-content imaging experiments on seipin-GFP stability upon cycloheximide treatment, non Adig-FLAG transfected cells (– Adig) were compared to cells with the highest 10% Adig-FLAG-expression in the Adig-FLAG-expressing cell pool (+ Adig).

Endogenous seipin-GFP and Adig-mScarlet3 interactions with emerging LDs were visualized in live A431 cells seeded and delipidated as described above. At 0 min, the cells were loaded with 200 µM oleic acid in the presence of HCS LipidTOX Deep Red (1:3000) in CO₂-independent medium (Gibco, no. 18045-054) and time-lapse confocal images were acquired after 20 min load at 403.5 msec intervals for 30 s with Leica Stellaris 8 microscope equipped with an environmental chamber.

For Perilipin 3 immunofluorescence, A431 cells with or without Adig-mScarlet3-expression were grown on coverslips, delipidated for 48 hours in 5% LPDS and loaded with 200 µM oleic acid for 30 min. The fixation and staining were performed as above with the following exceptions: the permeabilization was performed in 0.1% saponin in PBS, blocking in 10% FBS in PBS, Perilipin 3 antibody (Proteintech, no. 10694-1-AP, 1:200) and the Alexa Fluor 647-conjugated secondary antibody (Thermo Fisher Scientific, no. A31573, 1:200) were used. After the staining, the coverslips were mounted with Mowiol-DABCO. Perilipin 3 intensity was analyzed with Fiji by thresholding the

ACSL3-positive LDs in background subtracted images after which their total Perilipin 3 intensity was measured.

BPY-C12 incorporation into nascent LDs was performed as described previously (12). Briefly, ACSL3-GFP and Adig-HaloTag expressing A431 cells were seeded on fibronectin-coated LabTEK chambers (Thermo Fisher Scientific, no. 155411), delipidated for 3 days in 5% LPDS (last day +DGAT1 and 2 inhibitors, 5 µM each, Sigma-Aldrich, nos. PZ0207 and PZ0233), loaded with 200 µM OA for 30 min together with 700 nM JFX646-HaloTag ligand (Janelia Research Campus), washed twice with PBS and labeled with 1 µM BODIPY 558/568 C12 (Thermo Fisher Scientific, no. D3835) for 10 min and washed with PBS following with a 60 min chase in 200 µM OA in 5% LPDS-containing serum free medium and fixed as above. The cells were imaged immediately with a confocal Leica Stellaris 8 inverted microscope using 63x HC PL APO CS2 motCORR water objective NA 1.20. All the images captured with Leica Stellaris 8 were deconvolved with Huygens Professional (Scientific Volume Imaging). Lipid droplets were identified on the ACSL3-GFP channel with Ilastik and segmented in CellProfiler as described above. Nuclei were segmented manually in Fiji and used as seeds for segmenting cells in CellProfiler, using background signal on the GFP channel. On the Adig-Halo channel, mean intensity of 0.02 a.u. was used as a threshold for classifying cells as Adig-negative and Adig-positive. Total intensities (a.u.) of ACSL3-GFP and BPY-C12 in LDs per cell and total LD area (pixels, pixel size = 0.0081 µm²) per cell were measured in CellProfiler.

The fluorescence recovery after photobleaching (FRAP) assays were performed in live HeLa cells expressing both seipin-mNeonGreen and Adig-mScarlet3. The Förster resonance energy transfer (FRET) assays were performed in fixed HeLa cells expressing both seipin-mNeonGreen and Adig-mScarlet3.

Generation of yeast strains and plasmids

Saccharomyces cerevisiae was constructed in the genetic background of W303 (ade2-1; leu2-3; his3-11, 15; trp 1-1; ura3-1; can1-100). Deletion and tags of yeast genes were created using PCR-based homologous recombination via lithium acetate transformation. Proper chromosomal integrations were validated by PCR with primers flanking the open reading frame (ORF). Plasmids were generated via HiFi Assembly. The *Sei1*Δ strain was a gift from J. Goodman, and the *Sei1* ORF was replaced by a Hygromycin cassette. *Sei1*-mNeonGreen (*Sei1*-mNG) was generated using the longtine PLT plasmid cassette: PLT-mNeonGreen-Hygromycin (hygMX6). To generate strains in which mouse seipin was expressed at an endogenous expression level of *Sei1*, *msSeipin*-V5-mNeonGreen was used to clone into the longtine pFa6a series plasmid pFa6a-natMX, with the usage of restriction enzymes *AseI* and *BglII*. This plasmid was then used to replace the *Sei1* ORF with *msSeipin*-V5-mNeonGreen-NatMX, generating the *SEI1::msSeipin*-mNG strain. To express Adig in the yeast, Adig-FLAG-mScarlet3 was cloned into vectors pBp73C (CPY1 promoter, low expression) and pBp73G (GAP1 promoter, high expression), with the usage of restriction enzymes *XbaI* and *XhoI*. These Adig-expressing plasmids were transformed into yeast for exogenous expression, using a modified lithium acetate method.

Yeast fluorescence microscopy and image quantification

Cells were grown to logarithmic phase at 30°C in the appropriate synthetic medium, either with complete amino acids or -URA (transformation selection after plasmid transfection). To image lipid droplets, 1 ml of logarithmic growth culture was incubated with MDH (Abcepta, no. SM1000a) at a final concentration of 0.1 mM for 10 min before imaging. Cells on glass slides were imaged on the Nikon SoRa Spinning Disk microscope at 100x in room temperature. Z-series were captured at a step size of 0.4 µm and a total volume of 5.0 µm. The Nikon SoRa spinning disk microscope was purchased with a Shared Instrumentation grant from NIH: 1S10OD028630-01 to K. Luby-Phelps.

Linear adjustments for visualization purposes were made using ImageJ (NIH).

Every imaging experiment included at least three repeats, where at least three images from each imaging session were quantified using ImageJ. For each image, 20 cells were chosen at random, resulting in $n = 180$ cells for each sample. The diameter of LDs was quantified using ImageJ line and measure tools on brightfield images, also using MDH to verify LD identity. Any LDs with a diameter larger than $0.8 \mu\text{m}$ was considered as a super-sized lipid droplet. The intensity of Adig-mScarlet3 and Seipin-mNeonGreen were taken using the oval tool on the perimeter of each cell and measured in a single plane. Areas of Seipin-mNeonGreen and LD (MDH-stained) were quantified by default thresholding on max projected images.

Yeast lipid extraction, thin-layer chromatography (TLC), and TLC quantification

To maximize TAG accumulation, yeast was diluted to 0.1 OD_{600} from an overnight culture and grown for 24 hours at 30°C in the appropriate synthetic medium. Then 10 ml of medium was collected, and the wet weights of the pellets were normalized to the lowest value. Lipid extraction was performed using a modified Folch method (53). Cells were resuspended in water with 0.5-mm acid-washed glass beads (Sigma-Aldrich, no. G8772-500G) and lysed by three 1-min cycles on a MiniBeadBeater. Chloroform and methanol were added to the lysates, achieving a 2:1:1 chloroform:methanol:water ratio. Samples were vortexed and centrifuged to separate the organic solvent and aqueous phases, and the organic phase was collected. This procedure was repeated twice. The organic solvent phases were then combined and washed twice with 1 ml of 1.0 M KCl. Lipid samples were dried under argon gas and resuspended in chloroform to a final concentration of $1 \mu\text{l}$ of chloroform per 1 mg cell pellet wet weight.

Extracted lipids were spotted onto heated glass-backed silica gel 60 plates (Sigma-Aldrich, no. 1057210001) and neutral lipids were separated in an 80:20:1 hexane:diethyl ether:glacial acetic acid solvent. Each sample was spotted twice to control differences between loadings ($n = 5 \times 2, 10$). Each plate contained at least 5 spots of different concentrations of neutral lipid reference standard mixture (Nu-Chek Prep; no. 18-5C). The standard was prepared in chloroform to a final concentration of 10 mg/ml and diluted to $1 \mu\text{g}/\mu\text{l}$ before loading onto the plate. All TLC bands from both standards and samples were visualized by spraying dried plates with cupric acetate in 8% phosphoric acid and baking at 145°C for at least 30 min.

Baked TLC plates were scanned and processed for quantification using Image J. Using the rectangle and measure tools, the band intensity was taken from the neutral lipid standards to create a standard curve where the x-axis could be used to calculate the lipid mass in micrograms. Sample band intensities were then plotted on these standard curves to calculate the lipid mass in each sample. For every replicate, the raw value of lipids in experimental samples were normalized to the ones in the wild type.

Northern blot

As described before (54), RNA was extracted from different tissues and 3T3-L1 cells at the indicated differentiation stage. A total of $1 \mu\text{g}$ RNA was separated on a formaldehyde/agarose gel and transferred onto Biotrans nylon membrane. The blots were hybridized with ^{32}P -labeled probes recognizing Adig and Actin transcripts.

Plasmids

For transient overexpression, the open reading frame of mouse Adig (NM_145635.2) was cloned into pcDNA3.1(+) (Thermo Fisher Scientific, no. V79020) with either a C-terminal FLAG tag, C-terminal FLAG tag, and EGFP, or N-terminal EGFP and C-terminal FLAG tag. The Adig was also fused to a C-terminal mScarlet3 or HaloTag in a construct containing a weak PGK promoter in some experiments.

The open reading frame of mouse seipin, long isoform (Bsc12; NM_001136064.3) was cloned into pcDNA3.1(+) with either a C-terminal Myc tag or V5 tag. The open reading frame of mouse Gpat4 was cloned into pcDNA3.1(+) with either a C-terminal or N-terminal HA tag. An ER-mCherry-KDEL construct was assembled from a calreticulin-derived ER translocation signal, mCherry, and a KDEL ER retention signal and cloned into pcDNA3.1(+). pEGFP-C3 was obtained from TaKaRa (no. 6082-1).

For AAV production, EGFP, NanoLuc (NLuc), Adig-FLAG, Adig-FLAG-APEX2, and a mito-mKeima construct composed of a COX8-derived mitochondria translocation signal and hmKeima8.5 (55) were cloned into a custom pAAVK CAG backbone, driving expression from a constitutive CAG promoter. EGFP, NLuc, and codon-optimized Cre recombinase (iCre) were cloned into a custom pAAVK EF1a backbone, driving expression from a constitutive EF1a promoter.

For protein complex expression and purification, Adig-FLAG and StrepII-seipin (long isoform, NM_001136064.3) were cloned into a custom pPRX-TW vector, driving expression from a constitutive CMV promoter.

AAV production for in vitro experiments

To produce adeno-associated viruses (AAVs) of the AAV2/DJ serotype (56), HEK293T cells grown in 15 cm dishes were cotransfected with pAAVK (6 μg), pHelper (12 μg ; Cell Biolabs, no. VPK-400-DJ), and pRepCap DJ (24 μg ; Cell Biolabs, no. VPK-400-DJ) in DMEM supplemented with 5% FBS, GlutaMAX, 100 U/ml penicillin and 100 mg/ml streptomycin, using PEI (linear, MW 25000; Polysciences, no. 23966-1) at a PEI:DNA mass ratio of 3:1. Supernatants were collected 3 days later, fresh medium was added, and supernatants were again collected 5 days post-transfection. Collected supernatants were combined and centrifuged to pellet debris. To precipitate AAVS, cleared supernatants were supplemented with 500 mM NaCl and 8% w/w PEG-8000, incubated overnight at 4°C , and centrifuged for 30 min at $4,000g$, 4°C . Pellets were resuspended in PBS (Thermo Fisher Scientific, no. 10010049), aliquoted, and stored at -80°C . A small aliquot of the produced AAVs was digested with DNaseI (New England Biolabs, no. M0303L) and qPCR was performed to determine AAV titers, using the primers 5'-GGAACCCCTAGTGATGGAGTT-3' and 5'-CGGCCTCAGTGAGCGA-3'. Linearized, purified pAAVK plasmid DNA was used to obtain a standard curve for quantification. Pre-adipocytes were transduced with AAVs 2 days before induction.

Fluorescence protease protection assay

The topology of Adig was determined by a fluorescence protease protection assay as described before (17). Briefly, plasmids Adig-EGFP or EGFP-Adig with ER-mCherry-KDEL were cotransfected into HeLa cells in 35 mm dish with coverslip (MatTek, no. P35G-1.5-10-C). Two days later, the medium was replaced with KHM buffer (110 mM potassium acetate, 20 mM HEPES, 2 mM MgCl_2 , pH 7.2). An image was taken on fluorescence microscope (Zeiss LSM880 Airyscan). Subsequently, the plasma membrane was permeabilized by 100 μM digitonin. One minute later, cells were incubated with 50 $\mu\text{g}/\text{ml}$ proteinase K in KHM buffer. And the fluorescence images were immediately taken in the time-lapse mode.

APEX2 staining and electron microscopy

The APEX2 staining protocol was adapted from previous publications (16). Adipocytes were fixed with 2.5% glutaraldehyde in cacodylate buffer (100 mM sodium cacodylate with 2 mM CaCl_2 , pH 7.4) for 60 min at 37°C . DAB tablets (Sigma, no. D5905) were dissolved in 1x PBS to a final concentration of 0.5 mg/ml. Before staining, 30% H_2O_2 was added to the solution to a final concentration of 10 mM. To prevent staining from the endogenous redox proteins, cells were incubated with the DAB solution without H_2O_2 for 10 min. Then, the DAB/ H_2O_2 solution was added, and the cells were stained on ice for 60 min. After washing the cells three times, they were imaged on a bright-field

microscope to confirm the activity of APEX2. Then the cells were processed for EM staining and sectioning in the Electron Microscopy Core Facility at UTSW.

Western blotting

As described before (57), total proteins were prepared from cells or tissues using RIPA buffer, supplemented with protease and phosphatase inhibitors (Thermo Fisher Scientific, no. 88669). For protein from adipose tissues, frozen tissues were first lysed in TNET buffer (50 mM Tris-HCl pH 8.0, 150 mM NaCl, 5 mM EDTA) with protease and phosphatase inhibitors (Thermo Fisher Scientific, no. A32961). After centrifuging, Triton X-100 was added to the supernatant to a final concentration of 1% and incubated on ice for 15 min. The cell lysate was spun again for 10 min at 13,000g. The “fat-cake” at the top and debris on the bottom of the lysate was discarded. Protein concentration was determined with BCA kits (Thermo Fisher Scientific, no. 23225). Equal amounts of protein were loaded onto 26-well Criterion TGX precast gels (Bio-Rad, 4-20%, no. 5671095) and transferred onto nitrocellulose membranes (Bio-Rad, no. 1704157). After blocking with 3% BSA for 2 hours at room temperature, membranes were incubated with primary antibodies overnight at 4°C, followed by incubation with fluorescent dye-labeled secondary antibodies for 2 hours and imaging with an Odyssey scanner (Li-Cor). The following antibodies were used: anti-GAPDH (Fitzgerald, no. 10R-G109A), anti-Actin (Santa Cruz, no. sc-47778), anti-perilipin-1 (PROGEN, no. G29), anti-PPAR γ (Santa Cruz, no. sc-7273), anti-FLAG (Sigma-Aldrich, no. F7425 and no. F1408), anti-V5 (Cell Signaling, no. 13202), anti-myc (Cell Signaling, no. 2278; Santa Cruz, no. sc-40), anti-human seipin (Cell Signaling, no. 23846), anti-mouse seipin (Abcam, no. ab106793), IRDye 800 CW goat anti-rabbit secondary antibody (Li-Cor, no. 925-32211), and IRDye 680 goat anti-mouse secondary antibody (Li-Cor, no. 926-68070). To raise a polyclonal antibody against Adig, the carboxyterminal peptides were coupled to BAS via the unique cysteine residue and injected into rabbits according to standard protocols.

Size-exclusion chromatography of cell lysates

Plasmids pcDNA3.1 seipin-V5, seipin-Myc or Adig-FLAG were first transfected into HEK293T cells with PEI (linear, MW 25000; Polysciences, no. 23966-1). After 48 hours, cells were collected and washed with 1x PBS. The cell pellet was snap-frozen with liquid nitrogen and stored at -80°C until further processing. Before conducting gel filtration, cell pellets were thawed on ice and suspended in lysis buffer (25 mM Tris-HCl pH 8.0, 150 mM NaCl, 1% digitonin) with protease and phosphatase inhibitors (Thermo Fisher Scientific, no. 88669). The cell lysates were incubated on ice for at least 30 min with intermittent shaking. After centrifuging twice at 15,000g for 8 min, the supernatant was collected and filtered through 0.2 μm filter (VWR, no. 28145-477) prior to loading onto columns for size exclusion chromatography. The supernatant was either applied to a HiLoad Superdex-75 column (no. GE28-9893-33) or a Superose 6 Increase column 10/300 GL (no. GE29-0915-96) with fractionation buffer (25 mM Tris-HCl pH 8.0, 150 mM NaCl, 0.025% digitonin). The fractions were analyzed by immunoblotting. To ensure consistency in gel filtration results, the experiments are strictly controlled in the following steps. First, the same number of cells were used across experimental groups. Typically, four 150-mm dishes of HEK293T cells were used per group for the HiLoad Superdex-75 column, and one or two 150-mm dishes for the Superose 6 Increase column. Second, the same volume of cell lysates was loaded onto the column. Three milliliters of cell lysis was loaded onto the HiLoad Superdex-75 column, and 0.5 ml onto the Superose 6 Increase column. Third, the elution from the HiLoad Superdex-75 column was fractionated by 2 ml, and the elution from the Superose 6 Increase column was fractionated by 0.5 ml. Lastly, in immunoblot analysis, two internal controls (Actin and GAPDH) were used to align fractions across different groups.

Regarding the method used to quantify bands in immunoblots, we first summed the signal intensities from fraction 18 to 39 to obtain the total amount of a specific protein. The proportion of each fraction was then calculated by dividing the intensity of that fraction by the total value. The immunoblots were captured by LI-COR imaging system, and the quantifications were analyzed in a software called Image Studio. The variations in band darkness across samples are due to the adjustments of brightness and contrast in Image Studio and therefore do not reflect the expression levels of a specific protein. Moreover, in this system the quantification values, generated by the software, remain unaffected, independent from the brightness/contrast adjustments.

Coimmunoprecipitation

For coimmunoprecipitation, cells were resuspended in lysis buffer (25 mM Tris-HCl, pH 8.0, 150 mM NaCl, 1% digitonin) containing protease and phosphatase inhibitors (Thermo Fisher Scientific, no. 88669). After incubation on ice for 30 min, cell lysates were centrifuged at 15,000g for 15 min. The supernatant was applied to a HiLoad Superdex-75 column (no. GE28-9893-33). The eluent was fractionated into 2 ml fractions. To eliminate unspecific binding, fractions were incubated with empty magnetic beads (Thermo Fisher Scientific, no. 78609) for 1 hour at 4°C. Then the anti-FLAG (Sigma, no. F7425) or anti-Myc (Santa Cruz, no. sc-40) antibodies and magnetic beads were added to the different fractions, and the mixtures were rotated at 4°C overnight. The beads were next washed with IP buffer (20 mM Tris-HCl pH 7.2, 100 mM NaCl, 1 mM EDTA, 10% glycerol, 0.1% NP-40, 1% Triton X-100) five times and finally incubated with 2x SDS-PAGE loading buffer for 5 min at 50°C.

Proteomics

To identify the Adig-interacting proteins, FLAG immunoprecipitation was performed in adipocyte lysates with and without Adig-FLAG expression. The protein samples were separated in SDS-PAGE gel and then sent to the Proteomics Core of UTSW for LC-MS/MS.

Seipin-Adig complex expression and purification

Complexes of seipin-Adig, were produced using the Expi293 Expression System (Thermo Fisher Scientific, no. A14635). Expi293F cells were grown in Expi293 Expression Medium (Thermo Fisher Scientific, no. A1435101) at 37°C, 5% CO₂, 125 rpm, in a water vapor-saturated atmosphere. Separate 100 ml cultures of 3×10^8 cells were transfected with 100 μg total of pPRX-TW-Adig-FLAG and pPRX-TW-StrepII-seipin (long or short isoform), using the ExpiFectamine 293 Transfection Kit (Thermo Fisher, no. A14524) according to the manufacturer's recommendations. In cases where multiple plasmids were cotransfected, the total amount of plasmid DNA was equally split among the used plasmids, except when indicated otherwise. Transfection Enhancers 1 and 2 were added 18 to 22 hours post-transfection. Cells were collected 96 hours post-transfection by centrifugation for 10 min at 500g, 4°C, snap-frozen in liquid nitrogen, and stored at -80°C .

For protein purification, as described before (14) the cells were thawed on ice and resuspended in lysis buffer (25 mM Tris-HCl pH 8.0, 150 mM NaCl, 1% digitonin) with protease and phosphatase inhibitors (Thermo Fisher Scientific, no. A32961). After incubation on ice for 30 min, cell lysates were centrifuged for 15 min at 15,000g, 4°C. The cell lysates were applied to a Strep-Tactin XT 4Flow column (iba, no. 2-5013-001). The column was washed and eluted using components of the Strep-Tactin XT Buffer Set (iba, no. 2-1043-000) according to the manufacturer's recommendations. The eluents were concentrated to 5 ml using Amicon Ultra Centrifugal Filters (Millipore Sigma, no. UFC8100). The protein complexes were further purified by size-exclusion chromatography on a HiLoad Superdex-75 column (Millipore Sigma, no. GE28-9893-33) utilizing chromatography buffer (25 mM Tris-HCl pH 8.0, 150 mM NaCl, 0.025% digitonin). The peak fractions were combined and concentrated to 1 mg/ml using Amicon Ultra Centrifugal Filters (Millipore Sigma, no. UFC8100) for EM grid preparation.

Electron microscopy sample preparation and cryo-EM data acquisition

Three microliters of Seipin/Adig complex at 1.55 mg/ml was applied to Quantifoil 400-mesh R1.2/1.3 grids coated with graphene oxide (Quantifoil, Micro Tools GmbH, Germany). The GO grids were purchased from EMS (cat. no. GOQ400R1213Cu100; lot no. 230116). The grids were stored at room temperature for approximately 1 year prior to the application of the samples for grid vitrification. The grids were glow discharged for 10 s at 10 mA 0.38 mbar using air in a PELCO easiGLOW (Ted Pella) prior to blotting for 3.5 s under 100% humidity at 4°C with a 0 blot force and 15 s wait time between sample application and blotting and then plunged into liquid ethane using Vitrobot Mark IV (Thermo Fisher Scientific). The filter paper used for blotting was purchased from Ted Pella [product no. 47000-100; 595 Filter Paper, 55/20 mm diameter (outer/hole)].

The cryo-EM data were acquired on a Titan Krios microscope (Thermo Fisher Scientific) equipped with the post-column BioQuantum energy filter (Gatan) connected to a K3 direct electron detector (Gatan). Cryo-EM data were collected using SerialEM in a super-resolution counting mode with a 20 eV energy filter slit. Movies were acquired at a pixel size of 0.4172 Å, with an accumulated total dose of 60 e⁻/Å² over 40 frames. The dose rate was set at around 21 e⁻/pixel/s. The defocus in data collection was set in the range of -1.5 to -3.0 µm. A total of 5,520 movies were collected and used for data processing (table S2).

Prior to the Krios data collection, a small dataset was collected on a 200kV Glacios microscope (Thermo Fisher Scientific) equipped with a K3 camera (Gatan). Same as the Krios session, SerialEM was used for data collection. Movies were collected in super-resolution counting mode of the K3 camera at a pixel size of 0.4385 Å, with an accumulated total dose of 60 e⁻/Å² over 60 frames. The dose rate was set at around 14 e⁻/pixel/s. The defocus in data collection was set in the range of -1.5 to -3.0 µm. A total of 929 movies were collected and used for data processing.

Cryo-EM data processing

Cryo-EM data were processed using CryoSPARC (58). Beam induced motion-correction and dose-weighting to compensate for radiation damage over spatial frequencies were performed using Patch Motion Correction in CryoSPARC with a binning factor of 2, resulting in a pixel size of 0.8344 Å/pixel for the micrographs for the Krios dataset and 0.877 Å/pixel for the Glacios dataset. Contrast Transfer Function (CTF) parameters were estimated using Patch CTF estimation in CryoSPARC. All default CryoSPARC parameters were used except when specified below.

For the pilot Glacios dataset, 882 micrographs were selected for further processing after exposure curation in CryoSPARC. First, particle picking was performed using the Blob Picker job with a minimum particle diameter of 150 Å and a maximum particle diameter of 200 Å. This resulted in 336,843 total picks. After inspection within CryoSPARC, 66,647 particles were extracted from the micrographs with a box size of 384 pixels scaled to 128 pixels (effective binning factor of 3). The criteria used for excluding particle picks were NCC (Normalized Cross Correlation) score >0.260, and Local Power score between -732.000 and 5153.000. Next, the 66,647 particles were subjected to one round of 2D classification in CryoSPARC into 50 classes. From these 50 classes, four classes with clear seipin features (a clear wheel-like molecule) were selected. These four classes contained 7677 particles. The class averages from these four selected classes were then used as templates to repick the particles from the 882 micrographs using the Template Picker job in CryoSPARC with a particle diameter set at 180 Å, resulting in 796,880 total picks. Again, these particle picks were then inspected, and 379,544 particles were included and extracted from the micrographs with a box size of 384 pixels scaled to 128 pixels. The criteria for particle inclusion were NCC >0.300 and Local Power score between 1317.000 and 2406.000. The extracted 379,544 particles were

then subjected to two rounds of 2D classification in CryoSPARC. Then, 58,782 particles were selected from the 2D classification jobs and were subjected to 3D analysis detailed below.

As both dodecameric and undecameric structures were observed from the 2D class averages, we performed separate Ab-Initio Reconstruction jobs to generate the references needed for subsequent 3D analysis. In one job, C12 symmetry was applied, and two classes were generated, with one class containing 43,242 particles showing clear features of a dodecameric complex. The other map was of poor quality and was used as a junk map in a subsequent job (see below). In the other job, C11 symmetry was applied, and two classes were also generated, with one class containing 42,402 particles showing clear features of an undecameric complex. Next, the 58,782 particles were subjected to a 3D Heterogeneous Refinement job using the two references as initial models with no symmetry applied, resulting in 33,626 particles in the dodecameric class and 25,156 particles in the undecameric class.

For the dodecameric complex, another round of 2D classification was performed and 14,827 particles were selected. These particles were then reextracted with 0.877 Å pixel size and 384 pixel box size and refined in a Non-Uniform Refinement job with C12 symmetry after global CTF refinement to 3.36 Å overall resolution.

For the undecameric complex, the 25,156 particles were subjected to one round of 2D classification, and 5,043 particles were selected. These particles were then combined with the 14,827 particles selected from the dodecameric complex and subjected to one round of 3D Heterogeneous Refinement with three references: one dodecamer from the aforementioned Ab-Initio Reconstruction job with C12 symmetry, one undecamer from the aforementioned Ab-Initio Reconstruction job with C11 symmetry, and the junk map mentioned above. Then, 7,813 particles were selected from this job that corresponded to the undecameric complex. These particles were then reextracted with 0.877 Å pixel size and 384 pixel box size and refined in a Non-Uniform Refinement job with C11 symmetry after global CTF refinement to 3.80 Å overall resolution.

Based on our approach, 3,739 particles from the dodecameric complex were reused for reconstructing the undecameric complex. Therefore, we did not interpret any of these maps from this pilot dataset. But rather, these maps were only used as templates (the dodecameric map) for particle picking for the Krios dataset, and as initial references (both maps) for 3D analysis in the Krios dataset.

For the Krios dataset, 5,330 micrographs were selected for further processing after exposure curation in CryoSPARC. The 3.36 Å dodecamer map from above was used as the template for particle picking using CryoSPARC for the Krios data. First, 50 2D projections were generated using CryoSPARC in a Create Templates job. Next, these 2D projections, low pass filtered to 20 Å, were used as templates for particle picking in a Template Picker job with a particle diameter of 180 Å. CryoSPARC uses distances in real space for template matching, avoiding the need to scale the different pixel sizes of the images. This resulted in 4,084,888 picks and only 1,306,558 remained after inspection, with the criteria of NCC >0.380, 969.000 < Local Power score < 1986.000. These particles were extracted with a box size of 384 pixels scaled to 128 pixels and were subjected to two rounds of 2D classification in CryoSPARC (sorted into 50 classes for each round), from which 332,176 particles were selected (fig. S4D). These particles were then subjected to one round of 3D Heterogeneous Refinement with no symmetry in CryoSPARC with both undecamer and dodecamer maps from the pilot dataset as initial references. The resulting undecameric map from this job was of lower reported resolution and was used as a junk model in a subsequent job (see below). Next, 2D classification (sorted into 50 classes) was performed on separate classes and the selected particles were combined and subjected to another round of 3D Heterogeneous Refinement with no symmetry. This time the junk map mentioned above was introduced for absorbing junk/damaged

particles in addition to the undecameric and dodecameric maps. Next, the classes for the undecamer and dodecamer were refined with C11 and C12 symmetry respectively in separate 3D Homogeneous Refinement jobs, followed by another round of separate 2D classification jobs (sorted into 50 classes) to further clean up the particle stacks. After global and local CTF refinements, the final sets of 17,212 particles for the undecamer and 32,123 particles for the dodecamer were separately refined with corresponding symmetry using the Non-Uniform Refinement method in cryoSPARC, resulting in reconstructions with overall resolution of 3.19 Å and 2.98 Å, respectively. In all 3D jobs, the default dynamic mask settings were used in CryoSPARC. Initial low pass filter to the maps were set to 20 Å for 3D Heterogeneous Refinement jobs and 30 Å to Homogeneous and Non-Uniform Refinement jobs in CryoSPARC by default. Iteration number was default to 20 for 2D classification jobs, whereas 3D jobs were performed until convergence with no iteration numbers set. The maps were sharpened using DeepEMhancer. All resolutions were reported according to the gold-standard Fourier shell correlation (FSC) using the 0.143 criterion (59). Local resolution was estimated using CryoSPARC. 3DFSC was calculated using the server at <https://3dfsc.salk.edu/>.

Model building

AlphaFold (60) models for both seipin and Adig were used as the initial model for model building using COOT (61) with the DeepEMhancer sharpened maps. First, models that fell outside of the map were manually removed, followed by rigid body fitting in UCSF ChimeraX. Next, the model for one asymmetric unit was copied to the other locations according to the symmetry in ChimeraX and the chains were merged in COOT. The model was subjected to iterations of real-space refinement in Phenix (62) with secondary structure and Ramachandran restraints. In Phenix Real-space refinement GUI, “minimization_global,” “rigid_body,” “local_grid_search,” and “nqh_flips” were checked for model refinement. In the “Rotamers...” pop-out window, the following options were selected: Fit “outliers_and_poormap,” Target “fix_outliers,” and Tuneup “outliers_and_poormap.” Number of processors for the refinement job was set to 4. All other settings were default. Model geometries were assessed with MolProbity as a part of the Phenix validation tools, the Molprobity server (63, 64) (<http://molprobity.biochem.duke.edu/>) as well as the PDB Validation server (www.wwpdb.org). Figures were prepared using ChimeraX.

Animals

All animal procedures were approved by the Institutional Animal Care and Use Committee (IACUC) of the University of Texas Southwestern Medical Center (UTSW). The animal protocol numbers are 2024-103559-G and 2024-103545-G. Mice were maintained in a light/dark cycle of 12/12 hours in temperature-controlled rooms. All mice had free access to water and food (Teklad, no. 2916).

To generate adipocyte-specific, inducible Adig overexpressing mice, we first generated a transgenic mouse for the expression of Adig under the control of seven tetracycline-responsive elements (TRE). The coding sequence of mouse Adig was subcloned into the pTRE vector and then linearized with restriction enzymes. The TRE-Adig DNA fragments were purified for pro-nuclear injection by the Transgenic core at UTSW. Multiple founders were received and screened for the transgene integration. We then crossed positive lines with the adiponectin-rtTA mice (65). Doxycycline-containing chow diet (600 mg/kg diet) was used to induce the transgene Adig expression in the double transgenic mice (fig. S19A). Single transgenic mice carrying either TRE-Adig or adiponectin-rtTA were used as negative controls. All the mice are in C57BL/6 background.

To generate adipocyte-specific, inducible Adig knockout mice, we generated the Adig flox mice in the Transgenic Core at UTSW. As illustrated in fig. S23A, the first and second exons were flanked by the

loxP sequence with additional restriction enzyme sites, which were introduced by CRISPR/Cas9-mediated recombination. The successful founders were crossed with adiponectin-rtTA/TRE-Cre double transgenic mice. A doxycycline-containing chow diet (600 mg/kg diet) was used to induce Adig knockout in the double-transgenic mice. Adiponectin-rtTA single-positive mice were used as controls. All the mice are in the C57BL/6 background.

To generate the adipocyte-specific Bsel2 knockout mice (seipin cKO), the Bsel2 flox mice (66) were crossed with Adiponectin-Cre mice. Seipin cKO mice were further crossed with Adig iTG mice to establish the Adig iTG/Seipin cKO mice. A doxycycline-containing chow diet (600 mg/kg diet) was used to induce Adig transgene expression.

Histology

Mouse interscapular brown adipose, epididymal white adipose and subcutaneous white adipose around lymph nodes were fixed in 10% neutralized formalin for 4 days. Subsequently, samples were embedded in paraffin, sectioned (5 µm thickness) and stained with hematoxylin and eosin. The size of lipid droplets and adipocytes from the Adig overexpressing mice was analyzed by the Adipose Tissue Analysis Toolkit (ATAT) (67) in ImageJ. The Watershed and particle analysis in ImageJ enabled the quantification of lipid droplet size in brown adipose tissues from Adig iAKO and control mice.

Measurement of triglyceride and cholesterol content and triglyceride profiling in BAT

Triglyceride and cholesterol content were measured in the Metabolic Phenotyping Core of UTSW Medical Center. Briefly, 100 mg of frozen brown adipose tissues was homogenized and total lipids were extracted with 2:1 chloroform-methanol mixture (v/v), dried under nitrogen, and dissolved in ethanol reagent buffer containing 3% Triton X-100. The concentrations of triglyceride cholesterol were determined by a colorimetric enzymatic assay (Thermo Fisher Scientific, no. TR13421 and no. TR22421).

For the lipidomic profiling, triglyceride was first extracted from brown adipose tissues. One hundred milligrams of tissue was grinded in TNET buffer (50 mM Tris-HCl pH 8.0, 150 mM NaCl, 5 mM EDTA, protease and phosphatase inhibitors) with a grinder (Sigma-Aldrich, no. D8938). Lipids were collected from the top of lysates after centrifugation. To determine the triglyceride profile, 1 µl of lipids was added to 250 µl of CH₂Cl₂ in a borosilicate 2.0 ml amber glass vial, vortexed until solubilized. Then 750 µl of MeOH was added to the mixture and 40 µl of 1,3-dipentadecanoyl-2-oleoyl (d7)-glycerol (100 µg/ml in EtOH, Avanti Polar Lipids, cat. no. 791648C). The resulting solution was then vortexed vigorously and diluted 1:100 in MeOH/ CH₂Cl₂ (3:1; v/v). 2.0 and 0.6 µl were injected in the LC-MS/MS system which consisted of a Nexera 40 series UHPLC coupled with an LCMS-9030 Q-TOF (Shimadzu Scientific Instruments, Columbia, MD). One MeOH blank injection was intercalated between sample injections. Triacylglycerol species were resolved on a reverse-phase C18 column as described by Rampler *et al.* (68). Triacylglycerols were identified as ammoniated adducts in positive ion mode (Putative identification of m/z at 5 ppm tolerance via cross-referencing with the LIPID MAPS database. The LIPID MAPS Lipidomics Gateway, <https://www.lipidmaps.org/>). The relative abundance of each triglyceride species as the ratio of the peak area of the substance to be measured to the peak area of the internal standard.

To determine triglyceride content in A431 cells, WT and pPGK-Adig-FLAG-mScarlet3-expressing cells were starved for 1 day in 5% LPDS before loading with 200 µM OA in 5% LPDS for 60 min. Then cells were washed once with PBS and collected in 2% NaCl. Lipids were extracted as described (69). Equal amounts of each sample were separated by TLC using a running solvent of hexane:diethyl ether:acetic acid (80:20:1). TAG amounts were quantified from charred TLC plates

using standards for triglyceride in Fiji. Two technical replicates in two independent experiments were analyzed for each condition.

Triglyceride clearance test

Intralipid (Sigma-Aldrich, no. I141) was administered to mice by gavage (15 μ l/g body weight) after fasting overnight or 6 hours. Blood was collected from the tail before and after lipid administration at different time points. Following serum extraction, the triglyceride concentrations were determined by Infinity Triglycerides Reagent (Thermo Fisher Scientific, no. TR22421).

³H-triolein uptake assay

After mice were fasting overnight, the [³H]-triolein (PerkinElmer, no. NET431001MC) was retro-orbitally injected into mice at a dose of 2 μ Ci per mouse in 100 μ l of 5% Intralipid (70). At 1, 2, 5, 10 and 15 min after injection, 10–15 μ l blood samples were collected from a tail cut in 20 s. Ten microliters of blood was mixed with a 5 ml scintillation cocktail in scintillation vials. Fifteen minutes after injection, different tissues, including BAT, sWAT, eWAT, heart, liver, and skeletal muscle, were collected and stored in 0.75 ml chloroform/methanol (2:1) solution at –80°C until further processing. Following homogenization of the tissues, 0.5 ml of 1 M CaCl₂ was added to the chloroform/methanol solution. After centrifuging for 15 min at 8000g the top aqueous phase (~0.75 ml, the oxidative products of lipids) was transferred into a scintillation vial containing 5 ml scintillation cocktail. The bottom chloroform phase (~0.5 ml, the incorporation products in lipids) was transferred into an empty scintillation vial and was dried under a fume hood before a 5 ml scintillation cocktail was added. Finally, the radioactivity of all samples was counted in a scintillation counter (PerkinElmer, Tri-Carb 2910 TR). Tissue lipid uptake = oxidative lipids + incorporated lipids.

Atomistic and coarse-grained MD simulations

Protein modeling: The partially resolved 2.98 Å cryo-EM structure of the seipin-Adig complex was modeled through an atomistic description. The missing N-terminal (aa 25–41) and C-terminal (aa 247–260) transmembrane helices of seipin as well as the C-terminal transmembrane segment (aa 26–50) of Adig were reconstructed into the cryo-EM structure using the PyMol software. The transmembrane regions were modeled as a regular right-handed α helix.

System setup: The modeled seipin/Adig complex was embedded in a multi-component lipid bilayer whose lipid profile mimics that of the endoplasmic reticulum (ER) using a protocol described in our previous work (31). The ER membrane model in question comprises 13 different types of lipids with varying degrees of unsaturation (PC, PI, PE, PS, PA) as well as small amounts of cholesterol and triglycerides (TAGs). First, 1.25 mol % TAGs were randomly distributed in a lipid membrane around the protein complex. The protein-membrane system was solvated, and counter ions were added to neutralize the system. In addition, 0.15 M KCl ions were added to mimic the physiological salt concentration in the cell cytosol. The resulting system was energy-minimized and equilibrated under NVT and NPT conditions.

The Adig-free seipin 12-meric oligomer was constructed by simply removing the Adig molecules from the seipin/Adig complex model. A membrane-embedded system of the Adig-free 12-meric oligomer was prepared using the same protocol as described above for the seipin/Adig complex.

A MARTINI (version 2.2) (71) coarse-grained representation of the membrane-embedded Adig-free seipin 12-meric complex was constructed from the atomistic model using a coarse-grained model of the ER bilayer as described in our previous work (31). To determine the extent to which Adig affects the ability of the seipin complex to capture surrounding TAGs into its lumen, we investigated this issue through simulations in a model ER bilayer containing 1.25 mol % TAG using stoichiometric ratios of seipin:Adig complex of 12:0, 12:2, 12:4, and 12:12.

To investigate whether Adig affects the assembly of seipin oligomers, we performed coarse-grained simulations of seipin and Adig in a 2:2 ratio in the ER bilayer without TAG.

Simulation parameters: Simulations for both atomistic and coarse-grained model systems were carried out using the GROMACS simulation package [version 2021.5 (72)]. In atomistic simulations, the Charmm36/m force field with virtual interaction sites (73) was used for proteins, lipids, water, and counter ions to enable the use of a larger integration time step of 4 fs. For water, we used the TIP3P model (74). Temperature was maintained at 310 K using the Nose-Hoover thermostat (75) with a coupling constant of 0.5 ps. The pressure was maintained at 1 atm using the Parrinello-Rahman barostat (76) with a coupling constant of 2 ps. The Verlet cutoff scheme was employed to update the neighbor list every 10 steps. The LINCS algorithm (77) was employed to constrain the covalently bonded hydrogen atoms. A value of 1.0 nm was used as a cutoff for van der Waals interactions and the short-range component of electrostatic interactions, while Particle Mesh Ewald (78) was used for treating the long-range component of electrostatics.

The MARTINI force field (version 2.2) was used in the coarse-grained simulations for proteins, lipids, water, and counter ions to investigate TAG capture. The MARTINI force field (version 3.0.0) was used to explore the formation of seipin-Adig oligomers (79). The Elastic network (EINeDyn) (80) was used to maintain the overall shape of the protein with an elastic bond force constant of 500 kJ mol⁻¹ nm⁻², and the lower and upper elastic bond cutoff at 0.5 and 0.9 nm, respectively. Temperature and pressure were maintained at 310 K and 1 atm using the V-rescale thermostat (81) and the Parrinello-Rahman barostat (76), respectively. A standard MARTINI water model was used with a relative dielectric constant of 15. A cutoff of 1.1 nm was used for electrostatic and van der Waals interactions. The integration time step was chosen as 20 fs.

All simulations of atomistic systems were carried out with three repeats (1 μ s each). The simulations of the coarse-grained systems were repeated five times (5 μ s each). In a separate simulation programmed to investigate the formation of seipin-Adig oligomers (2:2 ratio) using the MARTINI model, 60 simulations (3 μ s each) were carried out.

Analysis of simulation data: Standard GROMACS tools were used for analysis. VMD (82) was used for visualizing the trajectories and rendering images. Plots were generated using Matplotlib (83).

To monitor the change in the inner lumen symmetry of the seipin oligomer, we measured the diameter of the lumen using two parameters $d1$ and $d2$. Here, $d1$ denotes the distance between the C α atom of residue 159 from protomers 1 and 7, while $d2$ denotes the distance between the same residue from protomers 4 and 10 (see fig. S11D).

The rate of TAG clustering was measured using the protocol described in our previous work; the values for TAG clustering in the seipin 12-mer system and in the control system (ER bilayer without seipin oligomer) were obtained from our previous work (31).

Statistical analysis

Data are represented as mean \pm SEM. Two-tailed Student's t test was performed to compare differences between two groups. For multiple group comparisons with more than two variables, two-way ANOVA was conducted, followed by Sidak's multiple comparison test. A p value of <0.05 was considered statistically significant. Statistical analyses were performed using Graphpad Prism software 10.2.3.

REFERENCES AND NOTES

1. S. Yu *et al.*, Adipocyte-specific gene expression and adipogenic steatosis in the mouse liver due to peroxisome proliferator-activated receptor γ 1 (PPAR γ 1) overexpression. *J. Biol. Chem.* **278**, 498–505 (2003). doi: [10.1074/jbc.M210062200](https://doi.org/10.1074/jbc.M210062200); pmid: [12401792](https://pubmed.ncbi.nlm.nih.gov/12401792/)
2. Y. H. Hong *et al.*, Up-regulation of adipogenin, an adipocyte plasma transmembrane protein, during adipogenesis. *Mol. Cell. Biochem.* **276**, 133–141 (2005). doi: [10.1007/s11010-005-3673-0](https://doi.org/10.1007/s11010-005-3673-0); pmid: [16132694](https://pubmed.ncbi.nlm.nih.gov/16132694/)

3. J. Y. Kim, K. Tillison, C. M. Smas. Cloning, expression, and differentiation-dependent regulation of SMAF1 in adipogenesis. *Biochem. Biophys. Res. Commun.* **326**, 36–44 (2005). doi: [10.1016/j.bbrc.2004.10.200](https://doi.org/10.1016/j.bbrc.2004.10.200); pmid: [15567149](https://pubmed.ncbi.nlm.nih.gov/15567149/)
4. G. Ren, P. Eskandari, S. Wang, C. M. Smas. Expression, regulation and functional assessment of the 80 amino acid small adipocyte factor 1 (Smaf1) protein in adipocytes. *Arch. Biochem. Biophys.* **590**, 27–36 (2016). doi: [10.1016/j.abb.2015.09.019](https://doi.org/10.1016/j.abb.2015.09.019); pmid: [26427354](https://pubmed.ncbi.nlm.nih.gov/26427354/)
5. A. Alvarez-Guaita *et al.*, Phenotypic characterization of *Adig* null mice suggests roles for adipogenin in the regulation of fat mass accrual and leptin secretion. *Cell Rep.* **34**, 108810 (2021). doi: [10.1016/j.celrep.2021.108810](https://doi.org/10.1016/j.celrep.2021.108810); pmid: [33691105](https://pubmed.ncbi.nlm.nih.gov/33691105/)
6. K. M. Szymanski *et al.*, The lipodystrophy protein seipin is found at endoplasmic reticulum lipid droplet junctions and is important for droplet morphology. *Proc. Natl. Acad. Sci. U.S.A.* **104**, 20890–20895 (2007). doi: [10.1073/pnas.0704154104](https://doi.org/10.1073/pnas.0704154104); pmid: [18093937](https://pubmed.ncbi.nlm.nih.gov/18093937/)
7. W. Fei *et al.*, Fld1p, a functional homologue of human seipin, regulates the size of lipid droplets in yeast. *J. Cell Biol.* **180**, 473–482 (2008). doi: [10.1083/jcb.200711136](https://doi.org/10.1083/jcb.200711136); pmid: [18250201](https://pubmed.ncbi.nlm.nih.gov/18250201/)
8. Y. Tian *et al.*, Tissue-autonomous function of *Drosophila* seipin in preventing ectopic lipid droplet formation. *PLoS Genet.* **7**, e1001364 (2011). doi: [10.1371/journal.pgen.1001364](https://doi.org/10.1371/journal.pgen.1001364); pmid: [21533227](https://pubmed.ncbi.nlm.nih.gov/21533227/)
9. Z. Cao *et al.*, Dietary fatty acids promote lipid droplet diversity through seipin enrichment in an ER subdomain. *Nat. Commun.* **10**, 2902 (2019). doi: [10.1038/s41467-019-10835-4](https://doi.org/10.1038/s41467-019-10835-4); pmid: [31263173](https://pubmed.ncbi.nlm.nih.gov/31263173/)
10. J. Magré *et al.*, Identification of the gene altered in Berardinelli-Seip congenital lipodystrophy on chromosome 11q13. *Nat. Genet.* **28**, 365–370 (2001). doi: [10.1038/ng585](https://doi.org/10.1038/ng585); pmid: [11479539](https://pubmed.ncbi.nlm.nih.gov/11479539/)
11. H. Wang *et al.*, Seipin is required for converting nascent to mature lipid droplets. *eLife* **5**, e16582 (2016). doi: [10.7554/eLife.16582](https://doi.org/10.7554/eLife.16582); pmid: [27564575](https://pubmed.ncbi.nlm.nih.gov/27564575/)
12. V. T. Salo *et al.*, Seipin regulates ER-lipid droplet contacts and cargo delivery. *EMBO J.* **35**, 2699–2716 (2016). doi: [10.15252/emboj.201695170](https://doi.org/10.15252/emboj.201695170); pmid: [27879284](https://pubmed.ncbi.nlm.nih.gov/27879284/)
13. H. Arlt *et al.*, Seipin forms a flexible cage at lipid droplet formation sites. *Nat. Struct. Mol. Biol.* **29**, 194–202 (2022). doi: [10.1038/s41594-021-00718-y](https://doi.org/10.1038/s41594-021-00718-y); pmid: [35210614](https://pubmed.ncbi.nlm.nih.gov/35210614/)
14. R. Yan *et al.*, Human SEIPIN binds anionic phospholipids. *Dev. Cell* **47**, 248–256.e4 (2018). doi: [10.1016/j.devcel.2018.09.010](https://doi.org/10.1016/j.devcel.2018.09.010); pmid: [30293840](https://pubmed.ncbi.nlm.nih.gov/30293840/)
15. C. Wang, A sensitive and quantitative mKeima assay for mitophagy via FACS. *Curr. Protoc. Cell Biol.* **86**, e99 (2020). doi: [10.1002/cpcb.99](https://doi.org/10.1002/cpcb.99); pmid: [31876372](https://pubmed.ncbi.nlm.nih.gov/31876372/)
16. J. D. Martell, T. J. Deerinck, S. S. Lam, M. H. Ellisman, A. Y. Ting. Electron microscopy using the genetically encoded APEX2 tag in cultured mammalian cells. *Nat. Protoc.* **12**, 1792–1816 (2017). doi: [10.1038/nprot.2017.065](https://doi.org/10.1038/nprot.2017.065); pmid: [28796234](https://pubmed.ncbi.nlm.nih.gov/28796234/)
17. H. Lorenz, D. W. Hailey, C. Wunder, J. Lippincott-Schwartz, The fluorescence protease protection (FPP) assay to determine protein localization and membrane topology. *Nat. Protoc.* **1**, 276–279 (2006). doi: [10.1038/nprot.2006.42](https://doi.org/10.1038/nprot.2006.42); pmid: [17406244](https://pubmed.ncbi.nlm.nih.gov/17406244/)
18. J. Chen *et al.*, Pervasive functional translation of noncanonical human open reading frames. *Science* **367**, 1140–1146 (2020). doi: [10.1126/science.aay0262](https://doi.org/10.1126/science.aay0262); pmid: [32139545](https://pubmed.ncbi.nlm.nih.gov/32139545/)
19. D. M. Anderson *et al.*, A micropeptide encoded by a putative long noncoding RNA regulates muscle performance. *Cell* **160**, 595–606 (2015). doi: [10.1016/j.cell.2015.01.009](https://doi.org/10.1016/j.cell.2015.01.009); pmid: [25640239](https://pubmed.ncbi.nlm.nih.gov/25640239/)
20. J. Chung *et al.*, LDAF1 and seipin form a lipid droplet assembly complex. *Dev. Cell* **51**, 551–563.e7 (2019). doi: [10.1016/j.devcel.2019.10.006](https://doi.org/10.1016/j.devcel.2019.10.006); pmid: [31708432](https://pubmed.ncbi.nlm.nih.gov/31708432/)
21. I. G. Castro *et al.*, Promethin is a conserved seipin partner protein. *Cells* **8**, 268 (2019). doi: [10.3390/cells8030268](https://doi.org/10.3390/cells8030268); pmid: [30901948](https://pubmed.ncbi.nlm.nih.gov/30901948/)
22. Y. A. Klug *et al.*, Mechanism of lipid droplet formation by the yeast Sei1/Ldb16 seipin complex. *Nat. Commun.* **12**, 5892 (2021). doi: [10.1038/s41467-021-26162-6](https://doi.org/10.1038/s41467-021-26162-6); pmid: [34625558](https://pubmed.ncbi.nlm.nih.gov/34625558/)
23. D. Binns, S. Lee, C. L. Hilton, Q. X. Jiang, J. M. Goodman, Seipin is a discrete homooligomer. *Biochemistry* **49**, 10747–10755 (2010). doi: [10.1021/bi1013003](https://doi.org/10.1021/bi1013003); pmid: [21062080](https://pubmed.ncbi.nlm.nih.gov/21062080/)
24. V. T. Salo *et al.*, Seipin facilitates triglyceride flow to lipid droplet and counteracts droplet ripening via endoplasmic reticulum contact. *Dev. Cell* **50**, 478–493.e9 (2019). doi: [10.1016/j.devcel.2019.05.016](https://doi.org/10.1016/j.devcel.2019.05.016); pmid: [31178403](https://pubmed.ncbi.nlm.nih.gov/31178403/)
25. B. R. Cartwright, J. M. Goodman, Seipin: From human disease to molecular mechanism. *J. Lipid Res.* **53**, 1042–1055 (2012). doi: [10.1194/jlr.R023754](https://doi.org/10.1194/jlr.R023754); pmid: [22474068](https://pubmed.ncbi.nlm.nih.gov/22474068/)
26. C. Windpassinger *et al.*, Heterozygous missense mutations in BSLC2 are associated with distal hereditary motor neuropathy and Silver syndrome. *Nat. Genet.* **36**, 271–276 (2004). doi: [10.1038/ng1313](https://doi.org/10.1038/ng1313); pmid: [14981520](https://pubmed.ncbi.nlm.nih.gov/14981520/)
27. V. A. Payne *et al.*, The human lipodystrophy gene BSLC2/seipin may be essential for normal adipocyte differentiation. *Diabetes* **57**, 2055–2060 (2008). doi: [10.2337/db08-0184](https://doi.org/10.2337/db08-0184); pmid: [18458148](https://pubmed.ncbi.nlm.nih.gov/18458148/)
28. W. Fei *et al.*, Molecular characterization of seipin and its mutants: Implications for seipin in triacylglycerol synthesis. *J. Lipid Res.* **52**, 2136–2147 (2011). doi: [10.1194/jlr.M017566](https://doi.org/10.1194/jlr.M017566); pmid: [21957196](https://pubmed.ncbi.nlm.nih.gov/21957196/)
29. J. Abramson *et al.*, Accurate structure prediction of biomolecular interactions with AlphaFold 3. *Nature* **630**, 493–500 (2024). doi: [10.1038/s41586-024-07487-w](https://doi.org/10.1038/s41586-024-07487-w); pmid: [38718835](https://pubmed.ncbi.nlm.nih.gov/38718835/)
30. S. Kim *et al.*, Seipin transmembrane segments critically function in triglyceride nucleation and lipid droplet budding from the membrane. *eLife* **11**, e75808 (2022). doi: [10.7554/eLife.75808](https://doi.org/10.7554/eLife.75808); pmid: [35583926](https://pubmed.ncbi.nlm.nih.gov/35583926/)
31. X. Prasanna *et al.*, Seipin traps triacylglycerols to facilitate their nanoscale clustering in the endoplasmic reticulum membrane. *PLoS Biol.* **19**, e3000998 (2021). doi: [10.1371/journal.pbio.3000998](https://doi.org/10.1371/journal.pbio.3000998); pmid: [33481779](https://pubmed.ncbi.nlm.nih.gov/33481779/)
32. V. Zoni *et al.*, Seipin accumulates and traps diacylglycerols and triglycerides in its ring-like structure. *Proc. Natl. Acad. Sci. U.S.A.* **118**, e2017205118 (2021). doi: [10.1073/pnas.2017205118](https://doi.org/10.1073/pnas.2017205118); pmid: [33481779](https://pubmed.ncbi.nlm.nih.gov/33481779/)
33. A. Kassar *et al.*, Acyl-CoA synthetase 3 promotes lipid droplet biogenesis in ER microdomains. *J. Cell Biol.* **203**, 985–1001 (2013). doi: [10.1083/jcb.201305142](https://doi.org/10.1083/jcb.201305142); pmid: [24368806](https://pubmed.ncbi.nlm.nih.gov/24368806/)
34. A. V. Bulankina *et al.*, TIP47 functions in the biogenesis of lipid droplets. *J. Cell Biol.* **185**, 641–655 (2009). doi: [10.1083/jcb.200812042](https://doi.org/10.1083/jcb.200812042); pmid: [19451273](https://pubmed.ncbi.nlm.nih.gov/19451273/)
35. M. Pagac *et al.*, SEIPIN regulates lipid droplet expansion and adipocyte development by modulating the activity of glycerol-3-phosphate acyltransferase. *Cell Rep.* **17**, 1546–1559 (2016). doi: [10.1016/j.celrep.2016.10.037](https://doi.org/10.1016/j.celrep.2016.10.037); pmid: [27806294](https://pubmed.ncbi.nlm.nih.gov/27806294/)
36. J. Song *et al.*, Identification of two pathways mediating protein targeting from ER to lipid droplets. *Nat. Cell Biol.* **24**, 1364–1377 (2022). doi: [10.1038/s41556-022-00974-0](https://doi.org/10.1038/s41556-022-00974-0); pmid: [36050470](https://pubmed.ncbi.nlm.nih.gov/36050470/)
37. H. Y. Mak *et al.*, AGPAT2 interaction with CDP-diacylglycerol synthases promotes the flux of fatty acids through the CDP-diacylglycerol pathway. *Nat. Commun.* **12**, 6877 (2021). doi: [10.1038/s41467-021-27279-4](https://doi.org/10.1038/s41467-021-27279-4); pmid: [34824276](https://pubmed.ncbi.nlm.nih.gov/34824276/)
38. H. Zhou, S. M. Black, T. W. Benson, N. L. Weintraub, W. Chen, Berardinelli-Seip congenital lipodystrophy 2/seipin is not required for brown adipogenesis but regulates brown adipose tissue development and function. *Mol. Cell Biol.* **36**, 2027–2038 (2016). doi: [10.1128/MCB.01120-15](https://doi.org/10.1128/MCB.01120-15); pmid: [27185876](https://pubmed.ncbi.nlm.nih.gov/27185876/)
39. L. Liu *et al.*, Adipose-specific knockout of SEIPIN/BSCL2 results in progressive lipodystrophy. *Diabetes* **63**, 2320–2331 (2014). doi: [10.2337/db13-0729](https://doi.org/10.2337/db13-0729); pmid: [24622797](https://pubmed.ncbi.nlm.nih.gov/24622797/)
40. W. Chen *et al.*, Berardinelli-Seip congenital lipodystrophy 2/seipin is a cell-autonomous regulator of lipolysis essential for adipocyte differentiation. *Mol. Cell Biol.* **32**, 1099–1111 (2012). doi: [10.1128/MCB.06465-11](https://doi.org/10.1128/MCB.06465-11); pmid: [22269949](https://pubmed.ncbi.nlm.nih.gov/22269949/)
41. T. C. Walther, S. Kim, H. Arlt, G. A. Voth, R. V. Farese Jr., Structure and function of lipid droplet assembly complexes. *Curr. Opin. Struct. Biol.* **80**, 102606 (2023). doi: [10.1016/j.sbi.2023.102606](https://doi.org/10.1016/j.sbi.2023.102606); pmid: [37150040](https://pubmed.ncbi.nlm.nih.gov/37150040/)
42. A. Mizrak *et al.*, Single-molecule analysis of protein targeting from the endoplasmic reticulum to lipid droplets. *bioRxiv* 2024.08.2027.610018 [Preprint] (2024); <https://doi.org/10.1101/2024.08.2027.610018>
43. M. M. Talukder, M. F. Sim, S. O'Rahilly, J. M. Edwardson, J. J. Rochford, Seipin oligomers can interact directly with AGPAT2 and lipin 1, physically scaffolding critical regulators of adipogenesis. *Mol. Metab.* **4**, 199–209 (2015). doi: [10.1016/j.molmet.2014.12.013](https://doi.org/10.1016/j.molmet.2014.12.013); pmid: [25737955](https://pubmed.ncbi.nlm.nih.gov/25737955/)
44. V. Choudhary, O. El Atab, G. Mizzon, W. A. Prinz, R. Schneiter, Seipin and Nem1 establish discrete ER subdomains to initiate yeast lipid droplet biogenesis. *J. Cell Biol.* **219**, e201910177 (2020). doi: [10.1083/jcb.201910177](https://doi.org/10.1083/jcb.201910177); pmid: [32349126](https://pubmed.ncbi.nlm.nih.gov/32349126/)
45. S. Li, X. Prasanna, V. T. Salo, I. Vattulainen, E. Ikonen, An efficient auxin-inducible degron system with low basal degradation in human cells. *Nat. Methods* **16**, 866–869 (2019). doi: [10.1038/s41592-019-0512-x](https://doi.org/10.1038/s41592-019-0512-x); pmid: [31451765](https://pubmed.ncbi.nlm.nih.gov/31451765/)
46. X. N. Sun *et al.*, GPR84-mediated signal transduction affects metabolic function by promoting brown adipocyte activity. *J. Clin. Invest.* **133**, e168992 (2023). doi: [10.1172/JCI168992](https://doi.org/10.1172/JCI168992); pmid: [37856216](https://pubmed.ncbi.nlm.nih.gov/37856216/)
47. Y. A. An *et al.*, Dysregulation of amyloid precursor protein impairs adipose tissue mitochondrial function and promotes obesity. *Nat. Metab.* **1**, 1243–1257 (2019). doi: [10.1038/s42255-019-0149-1](https://doi.org/10.1038/s42255-019-0149-1); pmid: [31984308](https://pubmed.ncbi.nlm.nih.gov/31984308/)
48. C. Dumesnil *et al.*, Cholesterol esters form supercooled lipid droplets whose nucleation is facilitated by triacylglycerols. *Nat. Commun.* **14**, 915 (2023). doi: [10.1038/s41467-023-36375-6](https://doi.org/10.1038/s41467-023-36375-6); pmid: [36807572](https://pubmed.ncbi.nlm.nih.gov/36807572/)
49. Á. Szkalitsy *et al.*, Nuclear envelope-associated lipid droplets are enriched in cholesterol esters and increase during inflammatory signaling. *EMBO J.* **44**, 2774–2802 (2025). doi: [10.1038/s44318-025-00423-2](https://doi.org/10.1038/s44318-025-00423-2); pmid: [40195500](https://pubmed.ncbi.nlm.nih.gov/40195500/)
50. J. L. Goldstein, S. K. Basu, M. S. Brown, Receptor-mediated endocytosis of low-density lipoprotein in cultured cells. *Methods Enzymol.* **98**, 241–260 (1983). doi: [10.1016/0076-6879\(83\)98152-1](https://doi.org/10.1016/0076-6879(83)98152-1); pmid: [6321901](https://pubmed.ncbi.nlm.nih.gov/6321901/)
51. C. Sommer, C. Straehle, U. Köthe, F. A. Hamprecht, in *2011 IEEE International Symposium on Biomedical Imaging: From Nano to Macro* (IEEE, 2011), pp. 230–233.
52. A. E. Carpenter *et al.*, CellProfiler: Image analysis software for identifying and quantifying cell phenotypes. *Genome Biol.* **7**, R100 (2006). doi: [10.1186/gb-2006-7-10-r100](https://doi.org/10.1186/gb-2006-7-10-r100); pmid: [17076895](https://pubmed.ncbi.nlm.nih.gov/17076895/)
53. J. Folch, M. Lees, G. H. Sloane Stanley, A simple method for the isolation and purification of total lipides from animal tissues. *J. Biol. Chem.* **226**, 497–509 (1957). doi: [10.1016/S0021-9258\(18\)64849-5](https://doi.org/10.1016/S0021-9258(18)64849-5); pmid: [13428781](https://pubmed.ncbi.nlm.nih.gov/13428781/)
54. P. E. Scherer, S. Williams, M. Fogliano, G. Baldini, H. F. Lodish, A novel serum protein similar to C1q, produced exclusively in adipocytes. *J. Biol. Chem.* **270**, 26746–26749 (1995). doi: [10.1074/jbc.270.45.26746](https://doi.org/10.1074/jbc.270.45.26746); pmid: [7592907](https://pubmed.ncbi.nlm.nih.gov/7592907/)
55. Y. Guan *et al.*, Live-cell multiphoton fluorescence correlation spectroscopy with an improved large Stokes shift fluorescent protein. *Mol. Biol. Cell* **26**, 2054–2066 (2015). doi: [10.1091/mbc.E14-10-1473](https://doi.org/10.1091/mbc.E14-10-1473); pmid: [25877871](https://pubmed.ncbi.nlm.nih.gov/25877871/)

56. D. Grimm *et al.*, In vitro and in vivo gene therapy vector evolution via multispecies interbreeding and retargeting of adeno-associated viruses. *J. Virol.* **82**, 5887–5911 (2008). doi: [10.1128/JVI.00254-08](https://doi.org/10.1128/JVI.00254-08); pmid: [18400866](https://pubmed.ncbi.nlm.nih.gov/18400866/)
57. C. Li *et al.*, IRE1 α mediates the hypertrophic growth of cardiomyocytes through facilitating the formation of initiation complex to promote the translation of TOP-motif transcripts. *Circulation* **150**, 1010–1029 (2024). doi: [10.1161/CIRCULATIONAHA.123.067606](https://doi.org/10.1161/CIRCULATIONAHA.123.067606); pmid: [38836349](https://pubmed.ncbi.nlm.nih.gov/38836349/)
58. A. Punjani, J. L. Rubinstein, D. J. Fleet, M. A. Brubaker, cryoSPARC: Algorithms for rapid unsupervised cryo-EM structure determination. *Nat. Methods* **14**, 290–296 (2017). doi: [10.1038/nmeth.4169](https://doi.org/10.1038/nmeth.4169); pmid: [28165473](https://pubmed.ncbi.nlm.nih.gov/28165473/)
59. P. B. Rosenthal, R. Henderson, Optimal determination of particle orientation, absolute hand, and contrast loss in single-particle electron cryomicroscopy. *J. Mol. Biol.* **333**, 721–745 (2003). doi: [10.1016/j.jmb.2003.07.013](https://doi.org/10.1016/j.jmb.2003.07.013); pmid: [14568533](https://pubmed.ncbi.nlm.nih.gov/14568533/)
60. J. Jumper *et al.*, Highly accurate protein structure prediction with AlphaFold. *Nature* **596**, 583–589 (2021). doi: [10.1038/s41586-021-03819-2](https://doi.org/10.1038/s41586-021-03819-2); pmid: [34265844](https://pubmed.ncbi.nlm.nih.gov/34265844/)
61. P. Emsley, B. Lohkamp, W. G. Scott, K. Cowtan, Features and development of Coot. *Acta Crystallogr. D Biol. Crystallogr.* **66**, 486–501 (2010). doi: [10.1107/S0907444910007493](https://doi.org/10.1107/S0907444910007493); pmid: [20383002](https://pubmed.ncbi.nlm.nih.gov/20383002/)
62. D. Liebschner *et al.*, Macromolecular structure determination using x-rays, neutrons and electrons: Recent developments in Phenix. *Acta Crystallogr. D Struct. Biol.* **75**, 861–877 (2019). doi: [10.1107/S2059798319011471](https://doi.org/10.1107/S2059798319011471); pmid: [31588918](https://pubmed.ncbi.nlm.nih.gov/31588918/)
63. V. B. Chen *et al.*, MolProbity: All-atom structure validation for macromolecular crystallography. *Acta Crystallogr. D Biol. Crystallogr.* **66**, 12–21 (2010). doi: [10.1107/S0907444909042073](https://doi.org/10.1107/S0907444909042073); pmid: [20057044](https://pubmed.ncbi.nlm.nih.gov/20057044/)
64. C. J. Williams *et al.*, MolProbity: More and better reference data for improved all-atom structure validation. *Protein Sci.* **27**, 293–315 (2018). doi: [10.1002/pro.3330](https://doi.org/10.1002/pro.3330); pmid: [29067766](https://pubmed.ncbi.nlm.nih.gov/29067766/)
65. Z. Zhang *et al.*, Adipocyte iron levels impinge on a fat-gut crosstalk to regulate intestinal lipid absorption and mediate protection from obesity. *Cell Metab.* **33**, 1624–1639.e9 (2021). doi: [10.1016/j.cmet.2021.06.001](https://doi.org/10.1016/j.cmet.2021.06.001); pmid: [34174197](https://pubmed.ncbi.nlm.nih.gov/34174197/)
66. H. Zhou, C. Xu, H. Lee, Y. Yoon, W. Chen, Berardinelli-Seip congenital lipodystrophy 2/SEIPIN determines brown adipose tissue maintenance and thermogenic programming. *Mol. Metab.* **36**, 100971 (2020). doi: [10.1016/j.molmet.2020.02.014](https://doi.org/10.1016/j.molmet.2020.02.014); pmid: [32246911](https://pubmed.ncbi.nlm.nih.gov/32246911/)
67. J. J. Robino *et al.*, Adipose Tissue Analysis Toolkit (ATAT) for automated analysis of adipocyte size and extracellular matrix in white adipose tissue. *Obesity* **32**, 723–732 (2024). doi: [10.1002/oby.23992](https://doi.org/10.1002/oby.23992); pmid: [38321231](https://pubmed.ncbi.nlm.nih.gov/38321231/)
68. E. Rampler *et al.*, Simultaneous non-polar and polar lipid analysis by on-line combination of HILIC, RP and high resolution MS. *Analyst* **143**, 1250–1258 (2018). doi: [10.1039/C7AN01984J](https://doi.org/10.1039/C7AN01984J); pmid: [29431763](https://pubmed.ncbi.nlm.nih.gov/29431763/)
69. E. G. Bligh, W. J. Dyer, A rapid method of total lipid extraction and purification. *Can. J. Biochem. Physiol.* **37**, 911–917 (1959). doi: [10.1139/y59-099](https://doi.org/10.1139/y59-099); pmid: [13671378](https://pubmed.ncbi.nlm.nih.gov/13671378/)
70. T. Onodera *et al.*, Endogenous renal adiponectin drives gluconeogenesis through enhancing pyruvate and fatty acid utilization. *Nat. Commun.* **14**, 6531 (2023). doi: [10.1038/s41467-023-42188-4](https://doi.org/10.1038/s41467-023-42188-4); pmid: [37848446](https://pubmed.ncbi.nlm.nih.gov/37848446/)
71. S. J. Marrink, A. H. de Vries, A. E. Mark, Coarse grained model for semiquantitative lipid simulations. *J. Phys. Chem. B* **108**, 750–760 (2004). doi: [10.1021/jp036508g](https://doi.org/10.1021/jp036508g)
72. M. J. Abraham *et al.*, GROMACS: High performance molecular simulations through multi-level parallelism from laptops to supercomputers. *SoftwareX* **1–2**, 19–25 (2015). doi: [10.1016/j.softx.2015.06.001](https://doi.org/10.1016/j.softx.2015.06.001)
73. O. Guvench *et al.*, CHARMM additive all-atom force field for carbohydrate derivatives and its utility in polysaccharide and carbohydrate-protein modeling. *J. Chem. Theory Comput.* **7**, 3162–3180 (2011). doi: [10.1021/ct200328p](https://doi.org/10.1021/ct200328p); pmid: [22125473](https://pubmed.ncbi.nlm.nih.gov/22125473/)
74. P. Mark, L. Nilsson, Structure and dynamics of the TIP3P, SPC, and SPC/E water models at 298 K. *J. Phys. Chem. A* **105**, 9954–9960 (2001). doi: [10.1021/jp003020w](https://doi.org/10.1021/jp003020w)
75. D. J. Evans, B. L. Holian, The Nose–Hoover thermostat. *J. Chem. Phys.* **83**, 4069–4074 (1985). doi: [10.1063/1.449071](https://doi.org/10.1063/1.449071)
76. M. Parrinello, A. Rahman, Polymorphic transitions in single crystals: A new molecular dynamics method. *J. Appl. Phys.* **52**, 7182–7190 (1981). doi: [10.1063/1.328693](https://doi.org/10.1063/1.328693)
77. B. Hess, H. Bekker, H. J. C. Berendsen, J. G. E. M. Fraaije, LINCS: A linear constraint solver for molecular simulations. *J. Comput. Chem.* **18**, 1463–1472 (1997). doi: [10.1002/\(SICI\)1096-987X\(199709\)18:12<1463::AID-JCC4>3.0.CO;2-H](https://doi.org/10.1002/(SICI)1096-987X(199709)18:12<1463::AID-JCC4>3.0.CO;2-H)
78. T. Darden, D. York, L. Pedersen, Particle mesh Ewald: An N -log(N) method for Ewald sums in large systems. *J. Chem. Phys.* **98**, 10089–10092 (1993). doi: [10.1063/1.464397](https://doi.org/10.1063/1.464397)
79. P. C. T. Souza *et al.*, Martini 3: A general purpose force field for coarse-grained molecular dynamics. *Nat. Methods* **18**, 382–388 (2021). doi: [10.1038/s41592-021-01098-3](https://doi.org/10.1038/s41592-021-01098-3); pmid: [33782607](https://pubmed.ncbi.nlm.nih.gov/33782607/)
80. X. Periole, M. Cavalli, S.-J. Marrink, M. A. Ceruso, Combining an elastic network with a coarse-grained molecular force field: Structure, dynamics, and intermolecular recognition. *J. Chem. Theory Comput.* **5**, 2531–2543 (2009). doi: [10.1021/ct9002114](https://doi.org/10.1021/ct9002114); pmid: [26616630](https://pubmed.ncbi.nlm.nih.gov/26616630/)
81. G. Bussi, D. Donadio, M. Parrinello, Canonical sampling through velocity rescaling. *J. Chem. Phys.* **126**, 014101 (2007). doi: [10.1063/1.2408420](https://doi.org/10.1063/1.2408420); pmid: [17212484](https://pubmed.ncbi.nlm.nih.gov/17212484/)
82. W. Humphrey, A. Dalke, K. Schulten, VMD: Visual molecular dynamics. *J. Mol. Graph.* **14**, 33–38 (1996). doi: [10.1016/0263-7855\(96\)00018-5](https://doi.org/10.1016/0263-7855(96)00018-5); pmid: [8744570](https://pubmed.ncbi.nlm.nih.gov/8744570/)
83. J. D. Hunter, Matplotlib: A 2D graphics environment. *Comput. Sci. Eng.* **9**, 90–95 (2007). doi: [10.1109/MCSE.2007.55](https://doi.org/10.1109/MCSE.2007.55)

ACKNOWLEDGMENTS

We thank T. Gillette, S. Li, Y. A. An, S. Rong, X. Qi, and T. Long for comments and suggestions. We thank M. C. Lethe, P. Wu, A. Uro, and D. Xin for technical support. We thank W. Chen, X. Zeng, and C. Zhang for providing the Bsc12 floxed and adipocyte-specific knockout mice. For support with cryo-EM studies, we thank the Structural Biology Lab and Cryo-EM Core Facility at University of Texas Southwestern Medical Center (UTSW), which are supported by grant RP220582 from the Cancer Prevention & Research Institute of Texas (CPRIT). We thank the Electron Microscopy Core Facility at UTSW for the assistance in APEX2 staining and Biomedium Imaging Unit, supported by HiLIFE and Biocenter Finland, for support in light microscopy. We thank the Proteomic Core at UTSW for the identification of Adig-interacting proteins. We thank the mouse Transgenic Core at UTSW for the generation of TRE-Adig and Adig flox mice. We thank the Metabolic Phenotyping Core at UTSW for the lipidomic study and the measurements of triglyceride and cholesterol levels. We thank CSC – IT Center for Science Ltd. (Espoo, Finland) for providing computing resources to perform MD simulations. **Funding:** This study was supported by National Institutes of Health (NIH) grants R01-DK055758, R01-DK099110, R01-DK127274, P01-AG051459, and R01-DK131537 to P.E.S., as well as NIDDK-NORC P30-DK127984; NIH grants R00-AG068239 and R01-DK138038 to S.Z.; NIH grants 2R56-DK108773 and R01-DK136558 to D.Y.O.; NIH grants R35-GM119768 and R01-DK126887 to W.M.H.; American Diabetes Association grant 7-21-PDF-158 to Chao L.; Research Council of Finland grants (324929 and 363179), the Sigrid Juselius Foundation, Jane and Aatos Erkko Foundation, and Foundation Leducq grant 19CVDO4 to E.I.; Research Council of Finland grants (331349, 336234, and 346135), the Sigrid Juselius Foundation, Helsinki Institute of Life Science (HiLIFE) Fellow Program, the Lundbeck Foundation, and the Human Frontier Science Program (RGP0059/2019) to I.V.; and Instrumentarium Science Foundation, The Finnish Medical Foundation, and Maud Kuistila Memorial Foundation grants to L.V. **Author contributions:** Conceptualization: Chao L., E.I., P.E.S.; Methodology: Chao L., X.-N.S., J.-B.F., R.M.W., L.V., X.P., K.G., K.K., D.-S.K., M.K., W.K., Yang L., Y.H., E.I., I.V., Chen L.; Investigation: Chao L., X.-N.S., R.M.W., J.-B.F., L.V., K.G., Yan L., N.J., X.P., M.V., K.K., A.S., C.J., R.G., C.V., L.S., S.C., J.V., A.C., D.L.P., M.-Y.W., T.O., A.R.N.; Visualization: Chao L., X.-N.S., L.V., K.G., Yan L., K.K., X.P., M.V., O.V.; Funding acquisition: P.E.S., E.I., Z.V.W., I.V., W.M.H., D.Y.O., Chao L., L.V.; Project administration: P.E.S., J.M.G., Y.H.; Supervision: P.E.S., E.I., I.V., J.M.G., Z.V.W., W.M.H., D.Y.O.; Writing – original draft: Chao L.; Writing – review & editing: J.M.G., D.Y.O., J.-B.F., Chao L., L.V., S.Z., Z.V.W., K.K., W.K., R.M.W., Y.H., W.M.H., I.V., E.I., P.E.S. **Competing interests:** The authors have no competing interests. **Data and materials availability:** The 3D electron microscopy map and atomic structure models data have been deposited in the Electron Microscopy Data Bank under accession codes EMD-45301 for the seipin-Adig complex and EMD-45302 for the seipin complex. The corresponding coordinates have been deposited in the Protein Data Bank under accession nos. 9C8D for the seipin-Adig complex and 9C8E for the seipin complex. Detailed information for the cryo-EM data collection is included in table S2. **License information:** Copyright © 2025 the authors, some rights reserved; exclusive licensee American Association for the Advancement of Science. No claim to original US government works. <https://www.science.org/about/science-licenses-journal-article-reuse>

SUPPLEMENTARY MATERIALS

science.org/doi/10.1126/science.adr9755

Figs. S1 to S25; Tables S1 and S2; MDAR Reproducibility Checklist; Movies S1 to S5

Submitted 24 July 2024; resubmitted 26 May 2025; accepted 15 September 2025

10.1126/science.adr9755